

Applications of computation in acoustics: ultrasound bioeffects and underwater transmission loss uncertainty

by

Brandon Patterson



Dissertation proposal
submitted in partial fulfillment
of the requirements for the degree of
Doctor of Philosophy
Mechanical Engineering
University of Michigan
2016

Doctoral Committee:

Assistant Professor Eric Johnsen, Chair

Professor David Dowling, Mechanical Engineering, University of Michigan

Professor Bill Schultz, Mechanical Engineering, University of Michigan

Professor Doug Miller, Radiology, University of Michigan

©Brandon Patterson

2016

TABLE OF CONTENTS

| | |
|---|-----------|
| List of Figures | ii |
| List of Acronyms and Abbreviations | v |
| Abstract | vi |
| Chapter | |
| 1 Introduction | 1 |
| I Ultrasound bioeffects | 3 |
| 2 <i>Past work:</i> Theoretical microbubble Dynamics at capillary breaching thresholds | 4 |
| 2.1 Key figures | 5 |
| 2.2 Conclusions | 8 |
| 3 <i>Current work:</i> Diagnostic Ultrasound Induced Lung Hemorrhage | 9 |
| 3.1 Introduction | 9 |
| 3.2 methods | 13 |
| 3.3 Analysis | 17 |
| 3.4 Preliminary results and discussion | 20 |
| 3.5 Conclusions | 27 |
| 3.6 Future Work | 29 |
| II Estimating transmission loss uncertainty in uncertain ocean environments. | 31 |
| 4 <i>Past work:</i> Efficient estimation of the probability density function of transmission loss in uncertain ocean environments via area statistics | 32 |
| 4.1 Key figures | 33 |
| 4.2 Conclusions | 38 |
| Bibliography | 40 |

LIST OF FIGURES

| | | |
|-----|---|----|
| 2.1 | History of the bubble radius (top) and input-pressure waveform (bottom) for an essentially linear case (frequency: 1.5 MHz; peak y negative pressure: 0.35 MPa). No bioeffects are observed here. $R_0 = 1 \mu\text{m}$; solid: $G = 5 \text{ kPa}$; dashed: $G = 100 \text{ kPa}$; dotted: $G = 1 \text{ MPa}$ | 5 |
| 2.2 | History of the bubble radius (top) and input-pressure waveform (bottom) for a highly nonlinear case (frequency: 7.5 MHz; peak negative pressure: 6.0 MPa). Bioeffects are observed here. $R_0 = 1 \mu\text{m}$; solid: $G = 5 \text{ kPa}$; dashed: $G = 100 \text{ kPa}$; dotted: $G = 1 \text{ MPa}$ | 5 |
| 2.3 | Dependence of the bubble dynamics on the gas contents ($G = 100 \text{ kPa}$). (Left) History of the bubble radius for PFP (solid) and air (dashed). (Right) Maximum temperature for PFP (circles) and air (squares). $R_0 = 0.1 - 2 \mu\text{m}$; frequency: 1.5 - 7.5 MHz. | 6 |
| 2.4 | Dependence of the bubble dynamics on the frequency for $G = 100 \text{ kPa}$. $R_0 = 0.1 - 2 \mu\text{m}$; empty circles: no bioeffects; squares: bioeffects. (Left) Dimensionless (Left) and dimensional (Right) maximum bubble radius. | 6 |
| 2.5 | Dependence of the dimensionless maximum bubble radius on the frequency for $G = 5 \text{ kPa}$ (Left) and $G = 1 \text{ MPa}$ (Right). $R_0 = 0.1 - 2 \mu\text{m}$; empty circles: no bioeffects; squares: bioeffects. | 7 |
| | | |
| 3.1 | A schematic view of the physical problem (left) is shown next to a schematic view of initial setup and boundary conditions of the numerical experiments performed (right). A Diagnostic Ultrasound (DUS) pulse impinging from tissue onto a pulmonary alveolus is modeled as an acoustic wave impinging from water onto a sinusoidally perturbed water-air interface. | 13 |
| 3.2 | The initial pressure in the domain. The trapezoidal wave pressure is shown as a function of distance from the interface (Left). A DUS-like pulse wave is used for comparison (Right). | 15 |
| 3.3 | Density surface plots are used to show the interface throughout its evolution for the 10 MPa trapezoidal wave case. Areas of high density (i.e., water) are indicated in dark blue. Areas of low density (i.e., air) are indicated in white. | 22 |
| 3.4 | The interface amplitude (left) and circulation (right) histories corresponding to the 10 MPa trapezoidal waves are shown for $t \leq 25$. Indicated times, t_{1-4} , are the times at which different stages of the incoming trapezoidal pressure wave shown in Figure 3.2 first encounter the interface. | 23 |

| | | |
|-----|---|----|
| 3.5 | The interface amplitude (left) and circulation (right) histories corresponding to the 1(yellow), 5(orange), and 10(blue) MPa trapezoidal waves are shown for $t \leq 25$. The circulation history is normalized by the acoustic amplitude of the incoming wave to illustrate that circulation deposition by the compression wave scales linearly with p_a | 24 |
| 3.6 | The interface amplitude (left) and circulation (right) histories corresponding to the 5(orange) and 10(blue) MPa trapezoidal waves are shown for $t \leq 500$. To appropriately compare late time dynamics, time has been offset in the interface amplitude history such that the phase reversal appears to occur simultaneously in both simulations. Dashed lines are used to demonstrate the expected slope of pure circulation driven interface growth, based on Equation (3.12). | 25 |
| 3.7 | A surface plot of vorticity for the 10 MPa trapezoidal wave case, at time $t = 0.6$, during the middle of the interface-compression wave interaction (Left). Each term of the circulation generation equation (3.11) is plotted as a function of time: $(d\Gamma/dt)_{advective}$ (blue), $(d\Gamma/dt)_{compressible}$ (orange), $(d\Gamma/dt)_{baroclinic}$ (yellow), $(d\Gamma/dt)_{total}$ (purple, dotted) is plotted as a function of time (Right). | 26 |
| 3.8 | The interface amplitude (left) and circulation (right) histories for varying elevated static pressure durations or lag time Δx_{lag} between the expansion and compression waves. Here we show results for $\Delta x_{lag} = 35\lambda$ (blue), $\Delta x_{lag} = 25\lambda$ (orange), $\Delta x_{lag} = 20\lambda$ (yellow), $\Delta x_{lag} = 10\lambda$ (purple), $\Delta x_{lag} = 5\lambda$ (green), $\Delta x_{lag} = 0\lambda$ (light blue) | 27 |
| 3.9 | The dimensionless interface amplitude (left) and dimensionless circulation (right) histories corresponding to the a water-air interface disturbed by the US-like pulse shown in Figure 3.2. | 28 |
| 4.1 | Nominal bathymetry of the four uncertain ocean environments used in this study. The ordering goes from shallowest (1) to deepest (4). | 33 |
| 4.2 | Generic range-dependent ocean environment with five uncertain parameters: bathymetry offset Δz ; sound speed increment multiplier γ ; and seabed properties (density ρ_b , sound speed c_b , attenuation coefficient α_b). Here, all five are assumed to be range independent. The source depth is a constant $z_s = 137$ m. The point of interest for recovering the PDF of Transmission Loss (TL) is indicated by a black dot. The rectangle surrounding this dot nominally indicates the range-depth area utilized by the area statistics technique. | 34 |
| 4.3 | (Top) Example TL field for a $f_s = 200$ Hz source in environment 2 with a $40\lambda_s \times 10\lambda_s(rangexdepth)$ area statistics sample area centered at range-depth location $r = 5720$ m, $z = 240$ m. (Bottom-left) Expanded area statistics TL sample rectangle from the TL field shown above. (Bottom-right) Probability Distribution Function (PDF) of TL generated from the TL values collected in the sample area. | 35 |

- 4.4 Comparison of area-statistics (solid curve) and Monte Carlo (MC) (dashed curve) generated PDFs of TL in environment 2 at $r = 5720$ m and $z = 288$ m (a), and $r = 1140$ m and $z = 384$ m. In both panels, the L_1 -error is the jagged marked area. (Left) $L_1 = 0.21$. With the MC PDF assumed to be correct, the mean and standard deviation errors of the area statistics PDF is 1.23 dB and 1.02 dB, respectively. (Right) $L_1 = 0.503$. The mean and standard deviation errors are 0.86 dB and 1.92 dB, respectively. The area- statistics-estimated PDF of TL on the left is considered engineering-level accurate while that on the right is not. . . 36
- 4.5 TL fields for the four environments shown in Figure 4.1 with a $f_s = 200$ Hz source and markers indicating locations where area statistics and MC generated PDFs of TL were compared. White circles indicate locations where area-statistics results compare favorably with those from MC calculations ($L_1 \leq 0.50$). Black triangles indicate locations where such comparisons are unfavorable ($L_1 \geq 0.50$). 37

LIST OF ABBREVIATIONS & ACRONYMS

CEUS Contrast-Enhanced Ultrasound

DG Discontinuous Galerkin

DUS Diagnostic Ultrasound

IC Inertial Cavitation

LH Lung hemorrhage

MC Monte Carlo

PD Pulse Duration

PDF Probability Distribution Function

PRF Pulse Repetition Frequency

RMI Richtmyer-Meshkov Instability

TL Transmission Loss

US Ultrasound

ABSTRACT

Applications of computation in acoustics: ultrasound bioeffects and underwater transmission loss uncertainty

by

Brandon Patterson

Chair: Eric Johnsen

Numerical simulations are highly useful for approaching a wide range of problems within the field of acoustics. From submarine and whale sounds propagating across vast oceans to ultrasound striking microscopic bubbles in the blood stream behind layers of optically opaque tissue, there are a variety of contemporary acoustic problems with challenges that make them incredibly difficult or infeasible to investigate experimentally. Furthermore, many systems of acoustic interest such as the ocean and human body are immensely complex, rapidly changing, and poorly understood such that at any given time our best knowledge of the system is still fraught with uncertainty. Computation is used ~~overcome~~ the difficulties of experimentation, explore a range of possibilities in uncertain systems, and to obtain detailed information about physical quantities that are not readily measurable. In this work, we present advancements in two very different areas of acoustics, made possible through the use of computation.

In the first part of this work, we investigate two problems related to biological effects of medical Ultrasound (US). The use of US for diagnostic and therapeutic purposes has grown very quickly over the last few decades, as technological advancements have allowed us to use US for everything from drug delivery and destruction of unwanted tissue to ~~high quality real time~~ imaging of the internals of the human body. However, certain US procedures have been shown to cause unwanted biological effects that are still poorly understood because they occur on such small length and time scales that they cannot be directly observed as they occur in the body. We develop numerical models to investigate experimentally observed hemorrhage associated with Contrast-Enhanced Ultrasound (CEUS) and DUS of the lung. In doing so, we compare calculated cavitation bubble dynamics pertinent to CEUS to previously obtained experimental results to show that accepted thresholds for Inertial Cavitation (IC) are unlikely to be useful for predicting CEUS bioeffects. For the case of DUS of the lung, we propose a new physical damage mechanism based on ultrasonically-induced baroclinic torque at tissue air interfaces within the lungs. We perform analysis and simulations to demonstrate that ^{vii} given certain simplifying assumptions, predictable deformation of the interface occurs via the proposed mechanism. We conclude that it is a feasible injury mechanism, ~~worthy of future study~~.

In the second part of this work we develop area statistics, a computationally efficient





CHAPTER 1

Introduction

The purpose of this introduction is to set the stage for the proposed dissertation research. The problems we approach in this work are all problems of interest, current to the field of Acoustics. Broadly, acoustics is the study of sound. In practice, this study is not limited to just the kinds of sound that can be heard by humans, but rather any molecular scale vibrations traveling throughout a media. As sounds both natural and man-made are ubiquitous, it is a topic that has intrigued man for quite some and attracted much attention and study. As such, we have gained not only an understand the physical nature of sound, but have also learned to harness it as a tool. Because sound waves travel reflect, transmit, and scatter in a mathematically describable way, they are ideally suited for gathering information in certain situations. Because they carry mechanical energy that can be focused, concentrated, and in some instances converted into other types of energy, such as heat, they can also be a powerful tool for physically altering an environment. In some applications of interest, attempts to use acoustics to gather information, can unintentionally lead to physical modification of the system, such is the case when DUS for medical imaging leads to unintended biological effects, or ultrasound bioeffects as we will refer to them from here on out.

Many problems of contemporary acoustic interest present challenges that make them difficult to investigate completely through direct experimentation. Some problems, such as certain ultrasound bioeffects, often involve physical processes that occur over such small length and time scales that they cannot be directly observed. When these phenomena are replicated in simplified lab experiments, as they frequently are, physical quantities of interest, like stress, are not always readily measurable. Other problems may call for experiments that are prohibitively costly and time-intensive, as is often the case in underwater and ocean acoustics experiments which can require long cruises with extensive personnel and equipment. Furthermore, in complex acoustic environments like the ocean or human body, we rarely have sufficient information to precisely and accurately describe the system of interest without a high degree of uncertainty. In instances such as these, where direct experimentation is infea-

sible or unable to provide the desired information, carefully designed numerical experiments can be incredibly useful for providing insight into the problem at hand.

The unifying theme of the work presented here is the use of computation to approach modern problems in acoustics. The two main areas of research considered are Ultrasound (US) bioeffects and underwater acoustic uncertainty. In the first part of this work, we investigate two problems related to biological effects of medical US. Specifically, we simulate physics associated with CEUS and DUS of the lung, which have both been shown to be capable of causing hemorrhage in mammals, in order to investigate the damage mechanism behind each. In the second part of this work we develop and test area statistics, a computationally efficient method for estimating the PDF of acoustic TL in uncertain ocean environments, which is useful in naval applications. As these areas are appreciably different, we will refer the reader to later portions of this document and to the authors relevant submitted and published works for more detailed introduction and background on each problem.

Part I

Ultrasound bioeffects

CHAPTER 2

Past work: Theoretical microbubble Dynamics at capillary breaching thresholds

In this chapter we present work in which experimentally-measured Ultrasound (US) pulses are used to simulate US contrast agent microbubble dynamics. The pulses were previously used in experiments to determine capillary breaching thresholds in rat kidneys (Miller *et al.*, 2008). We compare the calculated bubble dynamics to the experimentally-determined bio-effects thresholds to investigate the use of theoretical Inertial Cavitation (IC) thresholds as a predictor for bioeffects. This work was published in the Journal of the Acoustical Society of America (Patterson *et al.*, 2012). Here we present the abstract, key figures, and conclusions of the published work.

2.0.1 Abstract

In order to predict bioeffects in contrast-enhanced diagnostic and therapeutic ultrasound procedures, the dynamics of cavitation microbubbles in viscoelastic media must be determined. For this theoretical study, measured 1.5-7.5 MHz pulse pressure waveforms, which were used in experimental determinations of capillary breaching thresholds for contrast-enhanced diagnostic ultrasound in rat kidney, were used to calculate cavitation nucleated from contrast agent microbubbles. A numerical model for cavitation in tissue was developed based on the Keller-Miksis equation (a compressible extension of the Rayleigh-Plesset equation for spherical bubble dynamics), with a Kelvin-Voigt constitutive relation. From this model, the bubble dynamics corresponding to the experimentally obtained capillary breaching thresholds were determined. Values of the maximum radius and temperature corresponding to previously determined bioeffect thresholds were computed for a range of ultrasound pulses and bubble sizes for comparison to inertial cavitation threshold criteria. The results were dependent on frequency, the gas contents, and the tissue elastic properties. The bioeffects thresholds were

above previously determined inertial cavitation thresholds, even for the tissue models, suggesting the possibility of a more complex dosimetry for capillary injury in tissue.

2.1 Key figures

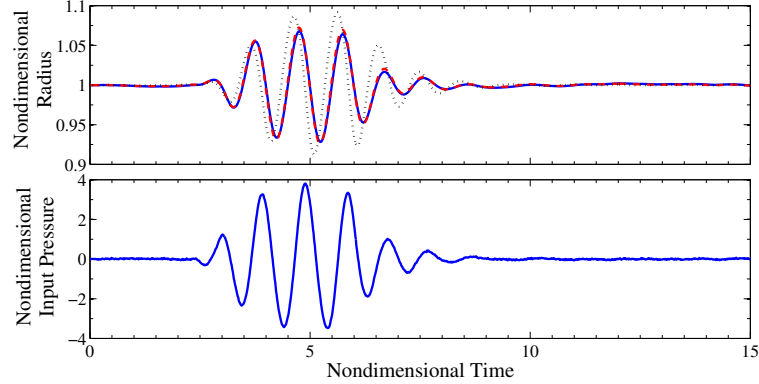


Figure 2.1: History of the bubble radius (top) and input-pressure waveform (bottom) for an essentially linear case (frequency: 1.5 MHz; peak y negative pressure: 0.35 MPa). No bioeffects are observed here. $R_0 = 1 \mu\text{m}$; solid: $G = 5 \text{ kPa}$; dashed: $G = 100 \text{ kPa}$; dotted: $G = 1 \text{ MPa}$.

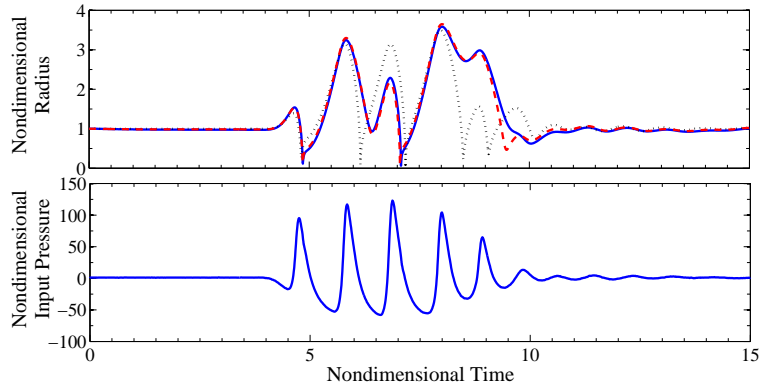


Figure 2.2: History of the bubble radius (top) and input-pressure waveform (bottom) for a highly nonlinear case (frequency: 7.5 MHz; peak negative pressure: 6.0 MPa). Bioeffects are observed here. $R_0 = 1 \mu\text{m}$; solid: $G = 5 \text{ kPa}$; dashed: $G = 100 \text{ kPa}$; dotted: $G = 1 \text{ MPa}$.

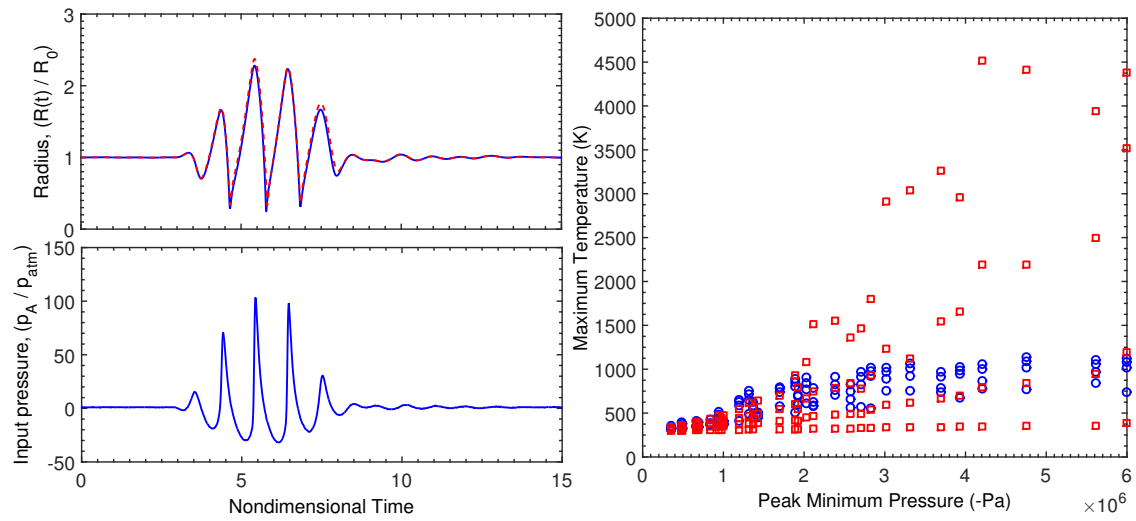


Figure 2.3: Dependence of the bubble dynamics on the gas contents ($G = 100$ kPa). (Left) History of the bubble radius for PFP (solid) and air (dashed). (Right) Maximum temperature for PFP (circles) and air (squares). $R_0 = 0.1 - 2 \mu\text{m}$; frequency: 1.5 - 7.5 MHz.

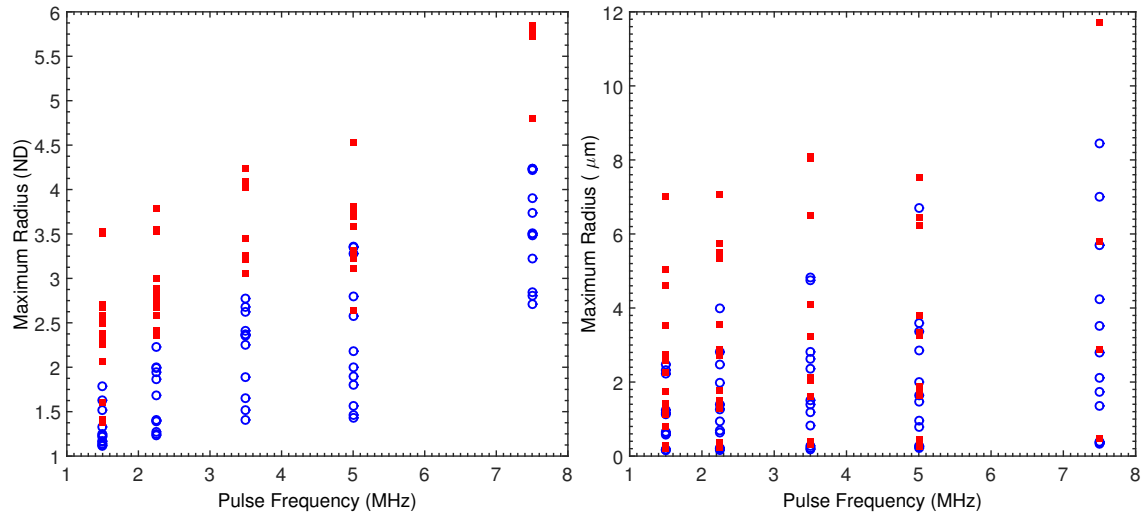


Figure 2.4: Dependence of the bubble dynamics on the frequency for $G = 100$ kPa. $R_0 = 0.1 - 2 \mu\text{m}$; empty circles: no bioeffects; squares: bioeffects. (Left) Dimensionless (Left) and dimensional (Right) maximum bubble radius.

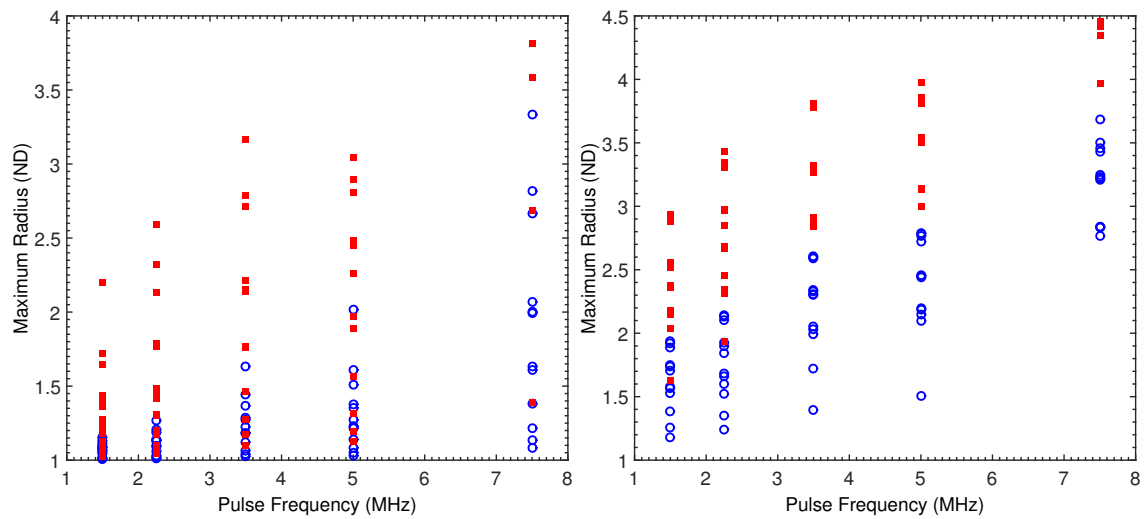


Figure 2.5: Dependence of the dimensionless maximum bubble radius on the frequency for $G = 5 \text{ kPa}$ (Left) and $G = 1 \text{ MPa}$ (Right). $R_0 = 0.1 - 2 \mu\text{m}$; empty circles: no bioeffects; squares: bioeffects.

2.2 Conclusions

In the present work, a numerical model is used to investigate experimentally observed bioeffects as a result of contrast-enhanced ultrasound. This work is unique in its combination of experimental results and numerical modeling. For the experimentally generated input pressure waveforms, it is known which of these triggered bioeffects, and from the numerical model we obtained calculated values for the dimensionless maximum radius and dimensional maximum temperature for each of these cases. By comparing the results of this study to previously established inertial cavitation thresholds used by [Apfel & Holland \(1991\)](#) and [Yang & Church \(2005\)](#), $T_{max} = 5000$ K and $R_{max} = 2$, it would appear that the inertial cavitation threshold does not play a role in determining the bioeffects threshold. However, it is unlikely that the inertial cavitation threshold is irrelevant. Instead, it is far more probable that these thresholds are not defined appropriately for cavitation in a viscoelastic medium, such as soft tissue. This work suggests the need for further experimental and numerical studies of cavitation in viscoelastic media.

The present work shows a strong correlation between cavitation dynamics and bioeffects when considering the pulse frequency. From the plot of maximum dimensionless radius vs. frequency, there is a clear separation between when bioeffects do and do not occur, and based on these results it appears that the frequency of the input pressure waveforms is of key importance to the definition of a bioeffect threshold, and likely the inertial cavitation threshold as well.

The present work shows that the elasticity of tissue significantly affects the bubble dynamics. This finding is perhaps not completely unexpected given that bubble dynamics are known to strongly depend on viscoelastic properties and model. The present study shows the need for more accurate measurements of material properties and for determining appropriate constitutive models for soft tissue, particularly at high strain rates. Finally, although the present work suggests that inertial cavitation collapse plays an important role with respect to bioeffects, it does not shed light on the exact mechanism, *e.g.*, shock emission upon collapse, growth beyond a given size, high temperatures generating free radicals, re-entrant jets in non-spherical collapse, etc. In future work we plan on investigating this injury mechanism by conducting direct simulations of the full equations of motion for bubble dynamics in a viscoelastic medium.

CHAPTER 3

Current work: Diagnostic Ultrasound Induced Lung Hemorrhage

3.0.1 Abstract

Over the past few decades, Diagnostic Ultrasound (DUS) of the lung has been shown to cause hemorrhage in a variety of mammals, though the underlying damage mechanism is yet to be determined. While this does not appear to be a medical problem of clinical significance, it is important to understand for the development of safe, new ultrasound procedures. In this work we propose a previously unconsidered physical damage mechanism for DUS-induced Lung hemorrhage (LH) – misalignments between ultrasound pressure gradients and tissue-air interface density gradients result in the generation of baroclinic vorticity. This drives the fragile cellular barriers around the alveoli to deform and ultimately hemorrhage. To test our hypothesis, we treat the lung as an inviscid, compressible fluid system and develop a simplified, numerical model of the problem to simulate DUS pulse-alveolus interaction. We show that acoustic waves, such as DUS pulses, are capable of generating ~~at~~ baroclinic vorticity at sharp liquid-gas interfaces such as those found in the lungs, and that this drives subsequent deformation of the interface. We propose a scaling law based on dimensional analysis to predict the growth of a purely circulation driven interface which we compare to growth observed in our numerical experiments to verify that vorticity is the mechanism responsible for the deformation.



3.1 Introduction

DUS is the safest form of medical imaging available today and has become ubiquitous in clinical practice. Currently, the only known bioeffect of non-contrast DUS known to occur in mammals is LH. The physical damage mechanisms underlying, DUS-induced LH are

presently unknown, though the damage does appear to be particularly severe, and is not considered a problem of significant clinical concern. However, it is an important problem to understand if we hope to improve lung DUS by expanding the US regimes used in clinical application. In this work, we use numerical experiments to investigate the underlying physics of DUS wave-lung interaction. We model the lung as a compressible multi-fluid system and solve the Euler equations of inviscid fluid motion to study the dynamics of fluid-fluid interfaces exposed to acoustic waves relevant to DUS. We observe that acoustically-generated vorticity at perturbed water-air interfaces drives the interface to deform. We hypothesize that a similar mechanism may be responsible for deforming and ultimately rupturing the fragile tissue barriers around alveoli, tiny air sacs within the lungs, leading to DUS induced LH.

Ultrasound (US)-induced LH is not a new problem. It was first discovered in mice over 20 year ago (Child *et al.*, 1990). Since then, the use of lung DUS has become increasingly common in certain critical care situations (Lichtenstein, 2009). And there has been much work to better understand the problem of DUS-induced LH. Previous research has primarily aimed at three specific ends: (1) Determining the dependence of damage characteristics and thresholds on the characteristics of the US subject; (2) Determining the dependence of damage characteristics and thresholds on the US properties; and (3) Investigating the physical damage mechanism causing the hemorrhage. Our work aims to contribute to this third area by investigating the fundamental physics underlying the problem.

Work in the first area has considered species, age, physiological development, and pulmonary state of the US subject as possible variables which DUS-induced LH may depend upon. Within mammals, DUS-induced LH has been observed to be largely species indiscriminant and has been found to occur in mice, pigs, rats, rabbits, and monkeys (Baggs *et al.*, 1996; Child *et al.*, 1990; Dalecki *et al.*, 1997; Frizzell *et al.*, 1994, 2003; Harrison *et al.*, 1995; Holland *et al.*, 1996; Kramer *et al.*, 2001; O'Brien & Zachary, 1997; O'Brien *et al.*, 2001a, 2003a, 2005, 2000, 2001c; Penney *et al.*, 1993; Raeman *et al.*, 1993, 1996; Tarantal & Canfield, 1994; Zachary & O'Brien, 1995; Zachary *et al.*, 2001a,b). While no direct experimentation has been performed on humans, for obvious ethical reasons, Meltzer *et al.* (1998) found that transesophageal echocardiography with similar US parameters to those causing lung hemorrhage did not lead to visible hemorrhage on the surface of the lung. Dalecki *et al.* (1997) investigated the effect of age on DUS-induced lung hemorrhage in mice by exposing neonatal, juvenile, and adult mice to DUS pulses. The study found that while hemorrhage thresholds were similar in all mice, the degree of hemorrhage was much greater in the adult mice than in the younger subjects. Similarly, O'Brien *et al.* (2003a), studied the age dependence of hemorrhage in pigs, and found that older pigs had a significantly lower hemorrhage

thresholds than juvenile and middle-aged pigs. In an unexpected result, the study also found that if one lung was exposed to US and the pig was then rolled over and the second lung exposed, the hemorrhage threshold in the second lung was substantially lower than in the first. In a separate study, O'Brien *et al.* (2002) subjected rats with variable degrees of lung inflation to DUS in order to study the role of the impedance boundary condition at the lungs pleural surface on LH. It was found that rats with deflated lungs, that had less impedance mismatch with their surroundings, were more easily damaged than deflated lungs.

The second area of research, investigating the dependence of lung hemorrhage on US properties, has seen the largest amount of work and is important for designing US in a way that is capable of high quality diagnostic imaging while minimizing any unwanted bioeffects. Research in this area has looked at the dependence of hemorrhage on US waveform and dosimetric properties. Zachary & O'Brien (1995) used continuous-wave and pulsed-wave US in mice, rabbits, and pigs, and found that while the continuous- and pulsed-wave-induced lesions appear macroscopically similar, they differ microscopically. Hemorrhage induced by continuous wave US consisted primarily of plasma and contained some cells, whereas pulsed-wave induced hemorrhage was composed largely of cells and contained little plasma. Raeman *et al.* (1996) subjected mice to pulsed US with varying exposure time and concluded that while threshold amplitudes appeared insensitive to exposure time, suprathreshold damage increased with increasing exposure. O'Brien *et al.* (2001b) investigated the effects of US beamwidth and found that as beamwidth increased so did the incidence, surface area, and volume of hemorrhage. It was noted that lung hemorrhage is perhaps the only known beamwidth-dependent mechanical bioeffect of US. O'Brien *et al.* (2003b) found evidence that increasing US pulse duration increases the likelihood of lung hemorrhage in rats.

While work in the third area of research, studying the cause of DUS-induced LH, has not yet led to a conclusive determination of the specific physical damage mechanisms, the most common ultrasound bioeffects mechanisms have been shown to be unlikely causes of the damage. Zachary *et al.* (2006) found that DUS-induced lung lesions do not appear similar to those induced by heat, and hence concluded that thermal damage mechanisms are unlikely. O'Brien *et al.* (2000) observed that the severity of DUS-induced LH in mice increased under raised hydrostatic pressure. And Raeman *et al.* (1996) notes that hemorrhage is unaffected by the introduction of US contrast agents into subjects. Both of these findings suggest that Inertial Cavitation (IC) is not a likely cause of DUS-induced LH. However, Holland *et al.* (1996) reports detecting cavitation during lung DUS of rats. Tjan & Phillips (2007, 2008) model DUS of the lung as an inviscid, free surface subjected to a Gaussian velocity potential and perform simulations to find that this setup can lead to the ejection of liquid droplets.

They go on to say that DUS of the lung may similarly lead to the ejected of droplets capable of puncturing the air-filled sacs within the lung. Despite these efforts, the precise damage mechanism underlying DUS-induced LH is still unknown.

Within the fluids community, there has been extensive research into the fundamental physics describing interactions between mechanical waves and fluid interfaces. Much of this research is motivated by applications in fusion energy and astrophysics and accordingly has investigated the Richtmyer-Meshkov Instability (RMI), in which a perturbed fluid-fluid interface is accelerated by a shock, causing the interface perturbation to grow (Drake, 2006). This growth is driven by a sheet of baroclinic vorticity deposited along the interface as a result of misalignment between the pressure gradient across the shock and the density gradient across the perturbed interface. Baroclinic vorticity is a nonlinear effect, the existence of which can be demonstrated by taking the curl of the conservation of momentum equation for a compressible fluid, however it cannot be explained by traditional linear acoustics.

We argue that the basic problem setup of the RMI, a mechanical wave impinging upon a material interface, is similar to DUS of the lungs. Furthermore, we postulate that because of the strong density discontinuity between air in the alveoli and the surrounding tissue, nonlinear fluid effects including baroclinic vorticity may be of significant importance to the dynamics of this system. Accordingly we propose another possible damage mechanism of DUS-induced LH. We hypothesize that misalignment between the pressure gradients in the DUS pulses and the density gradients across the tissue-air interfaces of the lungs creates a torque around the alveoli, which deforms and ultimately hemorrhages the alveolar walls.

The detailed nonlinear interactions between acoustic waves and perturbed fluid-fluid interfaces does not appear to have been previously studied in this manner or context. This work is separate from previous research into the RMI as a result of the acoustic waves being studied. Unlike shock waves, which occur over a few molecular mean free paths and interact nearly instantaneously, acoustic waves can occur over a much larger finite space. Consequently, their interaction with interfaces occurs over a longer period of time. The duration of which depends on a variety of factors including shape and amplitude of the waveform, the speed of sound in the media, and the relative orientation of the traveling wave and the interface (e.g., the shape of the interface). In this work we demonstrate that the finite duration of the wave-interface interaction can effect the qualitative behavior of the on interface dynamics because of the deformation that occurs during this period. We will specifically attempt to address the following questions:

1. Are acoustic waves capable of generating vorticity at perturbed fluid-fluid interfaces?

2. If so, by what mechanisms is vorticity generated?

3. what is the impact of the acoustic wave properties, such as amplitude and wave duration, on the vorticity and interface dynamics?

In the remainder of this work, we will first present a simplified model problem and a set of numerical experiments designed to investigate the fundamental physics underlying interactions between acoustic waves and perturbed interfaces between fluids. The simulation results and related analysis will be presented and discussed first in the context of the fluid dynamics. We will then draw from these results to further elaborate on the significance of these results as they regard to the motivating problem of DUS-induced lung hemorrhage. We will finally end by summarizing the main conclusions drawn from this work and suggest the next steps to be taken.

3.2 methods

In this section, we describe the set of numerical experiments performed to investigate the proposed questions. The experiments are designed to model the physics associated with a DUS pulse propagating from soft lung tissue onto a pulmonary alveolus. The dimensionless Euler equations of compressible, inviscid fluid motion are solved to simulate simplified trapezoidal acoustic waves propagating from water towards a sinusoidally perturbed water-air interface. The interface and vorticity dynamics are studied. To simulate the problem of interest, we consider a 2D, rectangular computational domain within the xy -plane. An acoustic wave impinges from water (top) downward toward air (bottom). The water-air interface is initially located at the origin and has a sinusoidal shape with wavelength λ and amplitude 0.03λ as seen in Figure 3.1. A single wavelength interface traverses the domain such that the domain is λ wide. This interface geometry is chosen be similar to previous studies of the RMI (Brouillette, 2002). At this point, it is also worth noting that because the dimensionless Euler equations are solved, no true physical length scale exists in the simulated system. Hence all length scales hereafter will be considered relative to an interface perturbation wavelength λ . Within the context of the DUS, λ can be thought of as a typical length scale of an alveolus.

While DUS motivates this study, our primary focus is still in studying the fundamental physics associated with acoustic waves interacting with perturbed fluid-fluid interfaces. As such, the non-linear, time-dependent nature of DUS pulse waveforms makes them far more complex than is necessary for our study. To simplify the problem and analysis, we initially use trapezoidal waveforms for the numerical experiments, in place of DUS pulses. Hence,

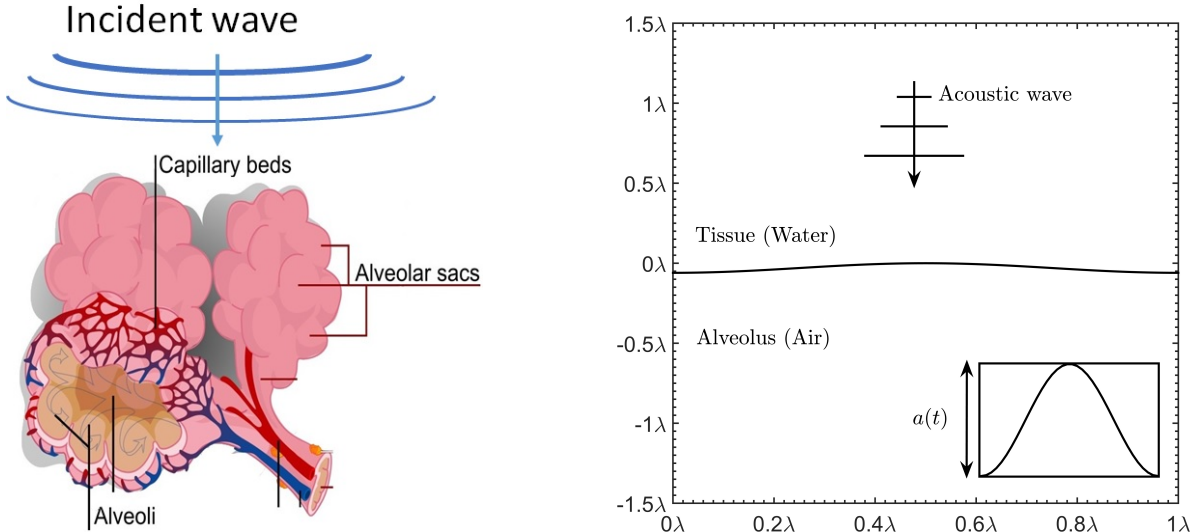


Figure 3.1: A schematic view of the physical problem (left) is shown next to a schematic view of initial setup and boundary conditions of the numerical experiments performed (right). A DUS pulse impinging from tissue onto a pulmonary alveolus is modeled as an acoustic wave impinging from water onto a sinusoidally perturbed water-air interface.

initially symmetric trapezoidal waveforms are used as seen in Figure 3.2. The waveform is composed of three stages, described here in the order that they encounter the interface. First, a compression wave occurs. Pressure increases linearly from atmospheric to a maximum of $p_a = 1, 5, \text{ or } 10 \text{ MPa gauge pressure}$. Second, the elevated pressure p_a remains constant over a fixed distance (or time). Finally, an expansion wave occurs. Pressure decreases linearly back to atmospheric pressure. The pressure rise and fall occur over equal distances 5λ , such that they have constant, equal slopes $\pm p_a/5\lambda$. Note that this neglects wave distortion due to acoustically induced changes in sound speed, which we assume to be small for our purposes. Unless otherwise stated, the period of constant pressure has length 35λ . Hence the total length of the incoming wave is 45λ .

To compare this setup to lung DUS, we assume a typical alveolar length scale $\lambda = 100 \mu\text{m}$. For the wave initially in water, ($c=1500 \text{ m/s}$), we find an equivalent acoustic pulse duration of our waveform is $3 \mu\text{s}$. This is within the range of typical US pulse durations in clinical imaging (Edelman, 2005) and relevant research (O'Brien, William D. et al., 2006).

To validate the relevance of the trapezoidal waveform and check the relevance of our results to the motivating problem, we perform simulations using a DUS-like pulse (see Figure 3.2). The waveform shape is composed of a sinusoidal pressure modulated by a Gaussian

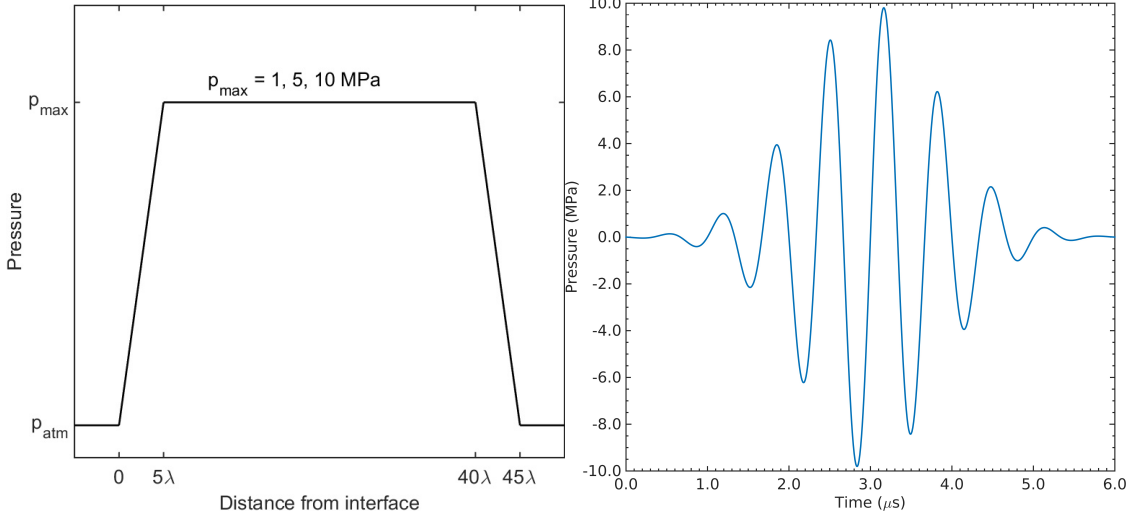


Figure 3.2: The initial pressure in the domain. The trapezoidal wave pressure is shown as a function of distance from the interface (Left). A DUS-like pulse wave is used for comparison (Right).

envelope,

$$p(t) = p_a \sin(2\pi f [t - t_0]) \exp\left(-\frac{t - t_0}{FWHM / (2\sqrt{2 \ln(2)})}\right). \quad (3.1)$$

Here $p(t)$ is the pulse pressure as a function of time, p_a is the maximum acoustic pressure, f is the frequency in Hz, t is time, t_0 is a time offset, and $FWHM$ is the full width at half maximum amplitude for the Gaussian envelope. The presented DUS-like pulse waveform is given as a function of time, as is typical of US. The speed of sound in water is used to convert this to a spatial waveform for the initial condition.

We solve the dimensionless Euler equations of compressible, inviscid fluid motion in two dimensions (x, y),

$$\frac{\partial \rho}{\partial t} + \frac{\partial(\rho u)}{\partial x} + \frac{\partial(\rho v)}{\partial y} = 0, \quad (3.2a)$$

$$\frac{\partial \rho u}{\partial t} + \frac{\partial}{\partial x} (\rho u^2 + p) + \frac{\partial}{\partial y} (\rho u v) = 0, \quad (3.2b)$$

$$\frac{\partial \rho v}{\partial t} + \frac{\partial}{\partial x} (\rho u v) + \frac{\partial}{\partial y} (\rho v^2 + p) = 0, \quad (3.2c)$$

$$\frac{\partial E}{\partial t} + \frac{\partial}{\partial x} [u(E + p)] + \frac{\partial}{\partial y} [v(E + p)] = 0, \quad (3.2d)$$

where t is time, ρ is density, p is the pressure, u and v are the velocity components in the x and y directions respectively, and E is the total energy. We use the density and sound speed of air to nondimensionalize the system. To close the system, we solve a stiffened equation of state which relate the total energy to the pressure and velocity in the flow, such that,

$$E = \frac{\rho(u^2 + v^2)}{2} + \frac{p + \gamma B}{\gamma - 1}. \quad (3.3)$$

Here B is a measure of liquid stiffness. For perfect gases, such as is our treatment of air, γ is the specific heats ratio and $B = 0$. It is worth noting that the sound speed in our simulations is calculated based on the following relationship, derived from the stiffened equation of state.

$$c = \sqrt{\frac{\gamma(p + B)}{\rho}}. \quad (3.4)$$

While physical diffusion is not considered in this setup, numerical diffusion does occur at fluid interfaces, creating a mixed region between the two fluids. To solve for the material parameters in the mixed region and prevent spurious pressure oscillations at the interface, two additional **advection equations** are solved for γ and B . Details of this implementation are explained by [Henry de Frahan *et al.* \(2015\)](#). The dimensional and dimensionless values of each fluid property can be found in tables 3.1 and 3.2 respectively. To solve the governing

Table 3.1: Dimensional properties of air and water used in simulations.

| | Density, ρ^* (kg/m ³) | γ | B^* (Pa) | c^* (m/s) ($p=1$ atm) |
|-------|---|----------|------------|--------------------------------|
| Air | 1.1765 | 1.4 | 0 | 347.23 |
| Water | 996 | 5.5 | 492115000 | 1648.7 |

* indicates dimensional parameter

Table 3.2: Dimensionless properties of air and water used in simulations.

| | Density, ρ | γ | B | c |
|-------|-----------------|----------|--------|------|
| Air | 1 | 1.4 | 0 | 1 |
| Water | 846.6 | 5.5 | 3469.1 | 4.75 |

Parameters are nondimensionalized by the density and sound speed of air.



equations, we implement a third-order accurate Discontinuous Galerkin (DG) scheme in space and a fourth-order accurate, adaptive Runge-Kutta method to march forward in time ([Henry de](#)

Frahan *et al.*, 2015). At this preliminary stage, we use both Roe and Rusanov, or local Lax-Friedrichs, approximate Riemann solvers. As previously stated, the computational domain width (x-direction) is λ . The domain length (y-direction) is 70λ . The grid resolution is 100 points per λ unless otherwise stated. To minimize artificial reflections, we use inflow and outflow boundary conditions at the top and bottom of the domain, and implement geometric grid stretching in the vertical direction for the top and bottom-most 10λ segments of the grid. Periodic boundary exist at the left and right edges of the domain.

3.3 Analysis

To answer the questions presented at the end of section , we perform analysis to make some predictions about the vorticity and interface dynamics of the system to be solved. The results of this analysis are later compared to the results of our numerical results in section 3.4 and discussed.

3.3.1 Vorticity generation order of magnitude analysis

To better understand vorticity generation within our problem we perform an order of magnitude analysis on each term of the vorticity generation equation for a 2D inviscid fluid system,

$$\frac{\partial \vec{\omega}}{\partial t} + (\vec{u} \cdot \nabla) \vec{\omega} = -\vec{\omega} (\nabla \cdot \vec{u}) + \frac{\nabla \rho \times \nabla p}{\rho^2}. \quad (3.5)$$

Each of these terms represents a different physical mechanism by which the vorticity in the system is changing, with the terms on the left side of the equation representing changes in the existing vorticity field and the terms on the right representing vorticity sources and sinks. The first term on the left represents the total change of vorticity at any given point in the flow field. The second term on the left represents the advection of vorticity within the field. The first term on the right describes stretching of vorticity due to compressibility in the flow. And the last term on the right is the baroclinic term which represents vorticity generated by the misalignment of the pressure and density gradients in the flow.

To perform the analysis, we assume that any vorticity generated will be a result of acoustic energy being convert to kinetic energy within the flow at and around the interface. As such specifically we consider the period in which the incoming compression wave encounters the interface. As this interaction occurs quickly, over an approximate time span $\Delta t_p \approx 5\lambda/c_w$, we assume that the interface is static and remains undeformed from its initial state during this

interaction.

To evaluate the vorticity in the compressible and advective terms, we write it as the curl of the velocity field $\vec{\omega} = \nabla \times \vec{u}$. Because the only motion in the flow is generated by the acoustic wave, we use acoustic relations to write the velocity as $u = \pm p/(\rho c)$. Lastly we treat gradient, curl, and divergence terms of any arbitrary quantity f such that $\nabla \cdot f = \mathcal{O}(= |f|/dY)$ and $\nabla \times f = |f|/dY$. Note that for our a uniform grid is used except where stretched at the top and bottom boundaries such that $dY = dX$ for our interests.

With these treatments and assumptions we can immediately approximate the order of the advective contribution to vorticity as

$$(\vec{u} \cdot \nabla) \vec{\omega} = \mathcal{O} \left(\left[\frac{|p|}{|\rho| |c|} \right]^2 \right), \quad \text{[Talk]}$$

and the compressible contribution as

$$-\vec{\omega} (\nabla \cdot \vec{u}) = \mathcal{O} \left(\left[\frac{|p|}{|\rho| |c|} \right]^2 \right). \quad \text{[Talk]}$$

In consideration of the baroclinic contribution to vorticity we expect the density gradient to be dominated by that across the interface. While the interface of our simulation is designed to obey thermodynamic conditions, and as such does not occur over a single dY , the thickness based on the distance from 5 to 95% volume fraction of water is initially $4.7 dY$ which we treat as $\mathcal{O}(dY)$. Additionally, to account for the degree of misalignment between the pressure and density gradients, we can rewrite the cross product as $|\nabla \rho| |\nabla p| \sin(\theta)$. Here θ is the angle between the direction of the acoustic pressure gradient which as being in the $+y$ -direction and the direction of the density gradient which we treat as the outward normal direction to the interface. Thus we estimate the order of the baroclinic vorticity generation rate as

$$\frac{\nabla \rho \times \nabla p}{\rho^2} = \mathcal{O} \left(\frac{|p| \sin(\theta)}{|\rho|} \frac{1}{dY^2} \right). \quad (3.8)$$

Recognizing that we expect the advective and compressible contributions to be of the same order, we compare them to the baroclinic term for the strongest point in the compression wave in which $p = p_a$ in water and $p = \mathbf{T} p_a$ in air. Here \mathbf{T} is the acoustic transmission coefficient, approximated based on sinusoidal plane wave impinging normally upon an interface as $\mathbf{T} = 2 [\rho c]_{air} / ([\rho c]_{air} + [\rho c]_{water})$ (Kinsler *et al.*, 1982). Here we note that we expect the majority of the generated vorticity will likely occur in the mixed-fluid interface region and that the

actual values will likely lie between those calculated for either pure fluid. To get an order of magnitude estimate for the baroclinic term we compute the mean $\overline{\sin(\theta)} \approx 0.12$ over the right half of the interface for our setup with $a_0 = 0.03\lambda$. Plugging in the dimensionless material values from Table 3.1 we approximate that for our minimum acoustic pressure, $p_a = 1$ MPa,

$$-\vec{\omega}(\nabla \cdot \vec{u}) \text{ and } (\vec{u} \cdot \nabla) \vec{\omega} = \begin{cases} \mathcal{O}(10^{-6} \frac{1}{dY^2}) & (\text{water}), \\ \mathcal{O}(10^{-5} \frac{1}{dY^2}) & (\text{air}), \end{cases} \quad (3.9a)$$

$$\frac{\nabla \rho \times \nabla p}{\rho^2} = \begin{cases} \mathcal{O}(10^{-4} \frac{1}{dY^2}) & (\text{water}), \\ \mathcal{O}(10^{-1} \frac{1}{dY^2}) & (\text{air}), \end{cases} \quad (3.9b)$$

and for our maximum acoustic pressure $p_a = 10$ MPa,

$$-\vec{\omega}(\nabla \cdot \vec{u}) \text{ and } (\vec{u} \cdot \nabla) \vec{\omega} = \begin{cases} \mathcal{O}(10^{-4} \frac{1}{dY^2}) & (\text{water}), \\ \mathcal{O}(10^{-3} \frac{1}{dY^2}) & (\text{air}), \end{cases} \quad (3.9c)$$

$$\frac{\nabla \rho \times \nabla p}{\rho^2} = \begin{cases} \mathcal{O}(10^{-2} \frac{1}{dY^2}) & (\text{water}), \\ \mathcal{O}(10^0 \frac{1}{dY^2}) & (\text{air}). \end{cases} \quad (3.9d)$$

Based on this order of magnitude analysis we expect two things. First, baroclinically generated vorticity is dominant over vorticity generated through all other mechanisms. Hence the quantities associated with this, such as acoustic pressure, are those of most interest to our study. Second, due to the relatively high density of water, we expect the majority of vorticity to occur in fluid with a higher volume fraction of air than water. Additionally, we expect that these trends will extend to considerations of the half-domain circulation γ , which is an integral quantity of vorticity ω .

To verify the above in our results, we will look for two things. First, as the above analysis suggests circulation generated during the compression wave-interface interaction is predominantly baroclinically generated. Because our acoustic pressure is linearly-increasing we predict that circulation deposited during this will also increase linearly with maximum acoustic pressure p_a , i.e.,

$$\Gamma \sim \frac{\nabla \rho \times \nabla p}{\rho^2} \sim p_a. \quad (3.10)$$

Second, to numerically verify our predictions for the types of vorticity generated in a visualizable way, we integrate the vorticity generation equation (3.5) over the half-domain.



$$\left(\frac{d\Gamma}{dt} \right)_{total} = \left(\frac{d\Gamma}{dt} \right)_{compressible} + \left(\frac{d\Gamma}{dt} \right)_{baroclinic} - \left(\frac{d\Gamma}{dt} \right)_{advective}, \quad (3.11)$$

Each term will be analyzed separately to determine the individual physical contributions to circulation at any point time. Here

$$\left(\frac{d\Gamma}{dt} \right)_{compressible} = - \int_{A_R} \vec{\omega} (\nabla \cdot \vec{u}) dA_R, \quad (3.11a)$$

$$\left(\frac{d\Gamma}{dt} \right)_{baroclinic} = + \int_{A_R} \frac{\nabla \rho \times \nabla p}{\rho^2} dA_R, \quad (3.11b)$$

$$\left(\frac{d\Gamma}{dt} \right)_{advective} = + \int_{A_R} (\vec{u} \cdot \nabla) \vec{\omega} dA_R, \quad (3.11c)$$

Finally, as we expect the interface growth to be purely circulation driven long after all waves have left the domain, we perform dimensional analysis to find a scaling law for the corresponding interface perturbation amplitude $a(t)$ as a function of circulation and time,

$$a(t) \sim \sqrt{\Gamma t}. \quad (3.12)$$

This proposed scaling law will be compared to the late time dynamics of the interface, after the acoustic wave has left the domain in Section 3.4.2.2.

3.4 Preliminary results and discussion

In this section we present the results of the numerical experiments and compare them to our analysis. We briefly touch on the general behavior of the acoustic waves, during the experiments, then go on to discuss the interface dynamics associated with the trapezoidal acoustic waves. We present results to illustrate the behavior of the interface during and after interactions with the acoustic waves. We compare the late time interface growth to the scaling law we obtained for purely circulation-driven interface growth based on dimensional analysis (Relationship (3.12)). We additionally provide plots of the half-domain circulation as a function of time and contours of vorticity to show that the compression and expansion waves deposit vorticity at the interface. We further plot the individual advective, compressible, and baroclinic contributions (3.11) to the circulation generation equation (3.11) as functions of time to

demonstrate the specific physical mechanisms responsible for generating circulation at each stage of the interaction. We next investigate the dependence of the interface and circulation dynamics on the time dependent features of the wave by varying the lag time between the compression and expansion portions of the trapezoidal wave. Then we present circulation and interface results for the US pulse-like waveform case for comparison to the trapezoidal wave cases. Lastly, we discuss broadly some of the implications of the results as a whole.

3.4.1 Acoustic wave behavior

Trapezoidal and US pulse-like waves (see Figure 3.2) propagate from water toward the perturbed water-air interface. Nearly all ($> 99.99\%$) of the acoustic energy is reflected back into the water. The sign of the reflected wave is opposite that of the incoming wave due to the movement of the incoming wave from media of higher to lower acoustic impedance, or simply, compression waves reflect expansion waves and vice versa. Due to the strong impedance mismatch, a very much weakened acoustic wave, with shape similar to the initial acoustic wave condition, is transmitted into the air. The curvature of the interface combined with the sound speed change across the interface causes slight redirection of the transmitted wave in accordance with Snell's law. Reflected and transmitted waves dissipate at the inflow and outflow boundaries.



3.4.2 Interface response to trapezoidal acoustic waves

3.4.2.1 Qualitative observations for the $p_a = 10$ MPa trapezoidal wave case

We first show typical interface amplitude and circulation histories to provide a qualitative understanding of the physics. For each trapezoidal wave case we observe that the interface begins to compress (i.e., the interface amplitude $a(t)$ decreases) when contacted by the wave and continues to deform throughout and after the interface-wave interaction period. At some point during this process the perturbation undergoes a phase change and the begins to grow in amplitude. Figure 3.3 shows snapshots of the interface at different points of its evolution for the case of a 10 MPa trapezoidal wave impinging on the water-air interface. Figure 3.4 shows the early-time interface amplitude and half-domain circulation histories for the same case. At $t_1 = 0^+$ the compression portion of the wave first hits the interface. The interface begins to compress and the perturbation amplitude decreases. From t_1 to t_2 the half-domain circulation Γ rises sharply. At $t_2 \approx 1.1$, the compression portion of the wave has passed, the interface amplitude continues to decrease. The half-domain circulation Γ stops its rapid growth and



changes little during this static elevated pressure period, until the expansion wave hits at t_3 . At $t \approx 5.0$, the perturbation undergoes a phase inversion and begins to grow. At $t_3 \approx 8.5$ the expansion wave first hits the interface. The perturbation amplitude continues to grow, and Γ increases sharply again. At $t_4 \approx 9.7$ the acoustic wave has finished traversing the interface, and atmospheric pressure is resumed.

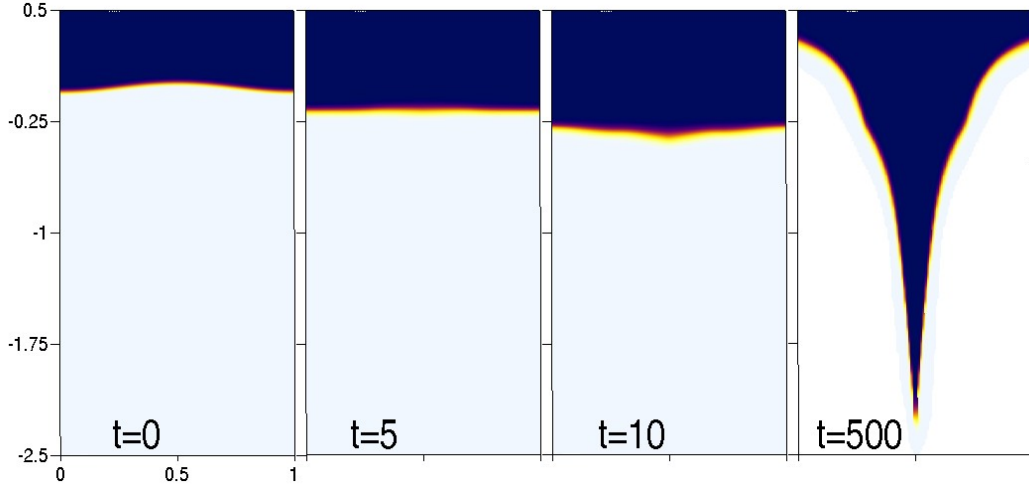


Figure 3.3: Density surface plots are used to show the interface throughout its evolution for the 10 MPa trapezoidal wave case. Areas of high density (i.e., water) are indicated in dark blue. Areas of low density (i.e., air) are indicated in white.

3.4.2.2 Dependence on wave amplitude

To illustrate the effects of varying the trapezoidal wave amplitude, while keeping the duration of each wave feature constant, we show interface amplitudes and half-domain circulation histories for $p_a = 1, 5$, and 10 MPa trapezoidal waves. In Figure 3.5, we look closely at the period around the wave interaction for $0 \leq t \leq 25$. We note that for the $p_a = 10$ MPa case, the phase reversal of the interface happened around $t = 5.0$, which is about half the time it took for this to occur for the $p_a = 5$ MPa case. The $p_a = 1$ MPa case, the evolution of the interface is sufficiently slow as to not phase invert during the period shown. For each wave amplitude, the circulation is normalized by the p_a to show that the circulation generated by the interface-compression wave interaction, $0^+ < t < scales < 0.12$, increases linearly with p_a . To show the longer term effects of varying amplitude and show the late time behavior of the interface, defined as the behavior significantly after the acoustic waves have left the domain, Figure 3.6 shows the interface amplitude and half-domain circulation histories for $0 \leq t \leq 500$ as functions of time for 5 and 10 MPa trapezoidal waves impinging on the interface. Here,

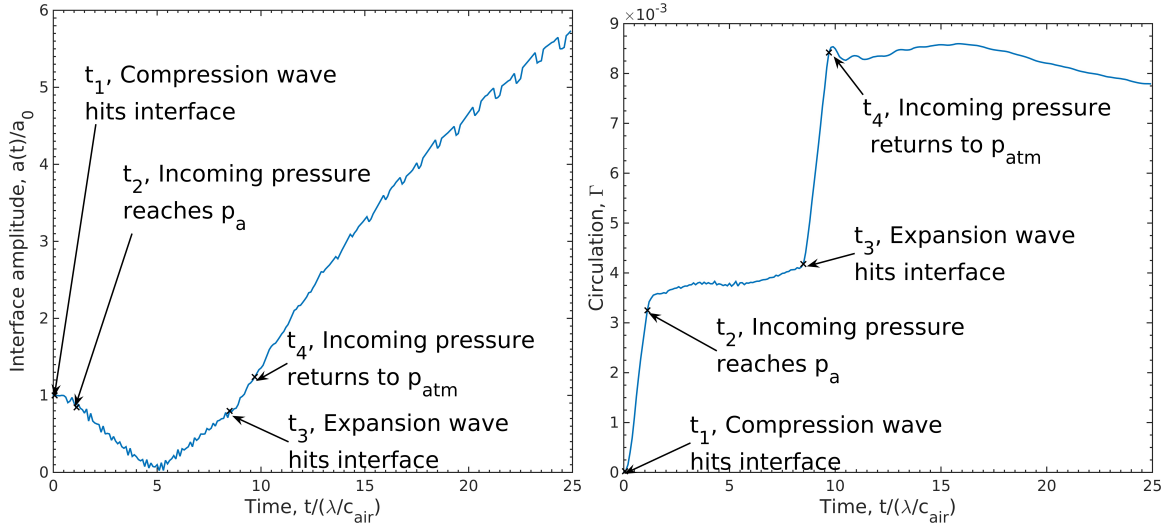


Figure 3.4: The interface amplitude (left) and circulation (right) histories corresponding to the 10 MPa trapezoidal waves are shown for $t \leq 25$. Indicated times, t_{1-4} , are the times at which different stages of the incoming trapezoidal pressure wave shown in Figure 3.2 first encounter the interface.

the interface amplitude is plotted on logarithmically-scaled axes and dashed lines are used to demonstrate the expected slope of purely circulation driven interface growth, based on Scaling law (3.12). For the 10 MPa wave case the slope of the observed growth appears to approach the predicted slope, though longer time simulations will be used to confirming this. Note that results for the 1 MPa trapezoidal wave were not included because the slow evolution of the interface made the computation prohibitively expensive.

3.4.2.3 Circulation and vorticity dynamics

We observe that the wave deposits a sheet of vorticity along the interface that moves with the interface in time. Figure 3.7 shows a surface plot of vorticity in the region of the domain around the interface for the 10 Mpa trapezoidal wave case, at $t = 0.6$, during the middle of the interface-compression wave interaction (Left). Not shown is the rest of the domain, where vorticity was relatively insignificant. The vorticity is antisymmetric across the $x = 0.5$ center line. To analyze the physical mechanisms generating the vorticity, we plot each term of the circulation generation equation (3.11) during the period around the wave-interface interaction. At $t = 0.6$, $(d\Gamma/dt)_{\text{advective}} = 2.9e - 5$; $(d\Gamma/dt)_{\text{compressible}} = -1.7e - 5$; $(d\Gamma/dt)_{\text{baroclinic}} = -8.6e - 3$; $(d\Gamma/dt)_{\text{total}} = -8.6e - 3$. Note that the baroclinic circulation generation rate traces the total circulation generation rate nearly exactly. This result is consistent with expected discrepancy based on our vorticity generation order of magnitude analysis (3.9).

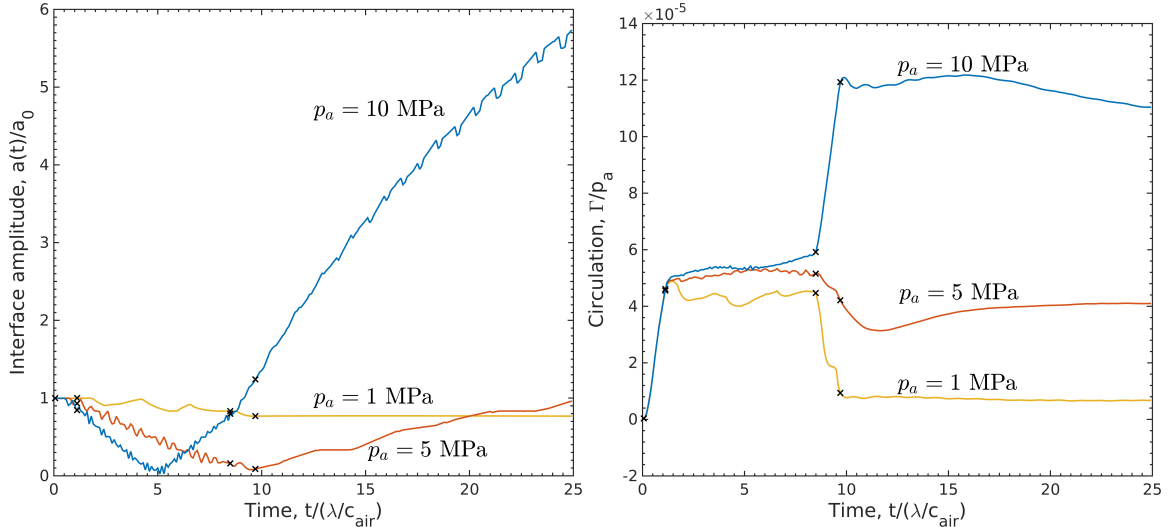


Figure 3.5: The interface amplitude (left) and circulation (right) histories corresponding to the 1(yellow), 5(orange), and 10(blue) MPa trapezoidal waves are shown for $t \leq 25$. The circulation history is normalized by the acoustic amplitude of the incoming wave to illustrate that circulation deposition by the compression wave scales linearly with p_a

3.4.2.4 Dependence on time-dependent wave features: time lag between compression and expansion waves

To demonstrate the importance of time-dependent wave features, we simulate $p_a = 10 \text{ MPa}$ trapezoidal waves of varying duration impinging onto the water-air interface. The compression and expansion portions of the waveform are exactly the same as is in the other trapezoidal wave cases, with pressure rising and falling over an initial distance of 5λ . We vary the duration of interaction between interface and the elevated static pressure portion of the wave, we will consider in terms of the static portion of the wave's initial length, defined as Δx_{lag} . We decrease this duration from the typical $\Delta x_{lag} = 35\lambda$ to $\Delta x_{lag} = 25\lambda, 20\lambda, 15\lambda, 5\lambda$, and 0λ . For each of these cases the system dynamics are virtually identical to the original case until the expansion encounters the interface. Figure 3.8 shows the interface amplitude and circulation histories for each case. For the three longest duration trapezoidal waves, with static elevated pressure durations of $\Delta x_{lag} = 35\lambda, 25\lambda$ and 20λ , we note that the expansion encounters the interface after the phase reversal has already occurred. In these cases, the expansion deposits additional circulation at the interface. For the shorter duration waves, with static elevated pressure durations of $\Delta x_{lag} = 10\lambda, 5\lambda$ and 0λ , the expansion encounters the interface before the phase inversion and the net half-domain circulation is decreased. We note that before or after the phase change of the interface, the larger $a(t)$ is at the time the expansion encounters the interface, the more circulation is generated by the wave, though this does not necessarily

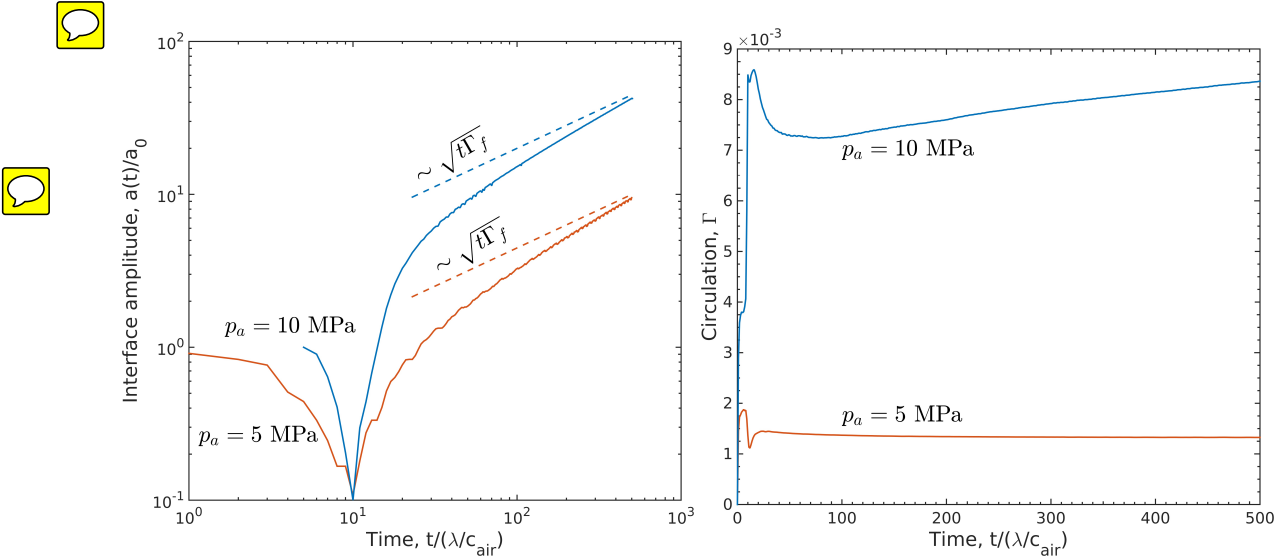


Figure 3.6: The interface amplitude (left) and circulation (right) histories corresponding to the 5(orange) and 10(blue) MPa trapezoidal waves are shown for $t \leq 500$. To appropriately compare late time dynamics, time has been offset in the interface amplitude history such that the phase reversal appears to occur simultaneously in both simulations. Dashed lines are used to demonstrate the expected slope of pure circulation driven interface growth, based on Equation (3.12).

hold true across the phase inversion.

3.4.3 Interface response to Diagnostic Ultrasound (DUS) waves

To evaluate the relevance of our trapezoidal wave experiments we simulate a $p_a = 1, 5$ and 10 MPa DUS pulse-like waves (See Figure 3.2) impinging onto the water air interface. In figure 3.9 we illustrate the circulation and interface amplitude histories for the $p_a = 10$ MPa DUS like-pulse case. The post-wave interface dynamics are similar to those observed for trapezoidal wave cases. During the wave-interface interaction, the interface amplitude is compressed overall, but oscillations are observed in correspondence with the acoustic pulse oscillations. After the wave has left the interface, the perturbation amplitude continues to decrease until the interface undergoes a phase inversion, after which the perturbation amplitude grows for the remainder of the simulation. half-domain circulation oscillates during wave-interface interaction before settling to a nearly constant non-zero value after the wave has passed. We note that the total circulation deposited is of the same order of magnitude as that generated by the trapezoidal wave of the same amplitude and duration. Qualitatively similar results were observed for the 5 MPa case. For the one 1 MPa case, the evolution of the system was slow such that running the simulation long enough to obtain useful results was computationally

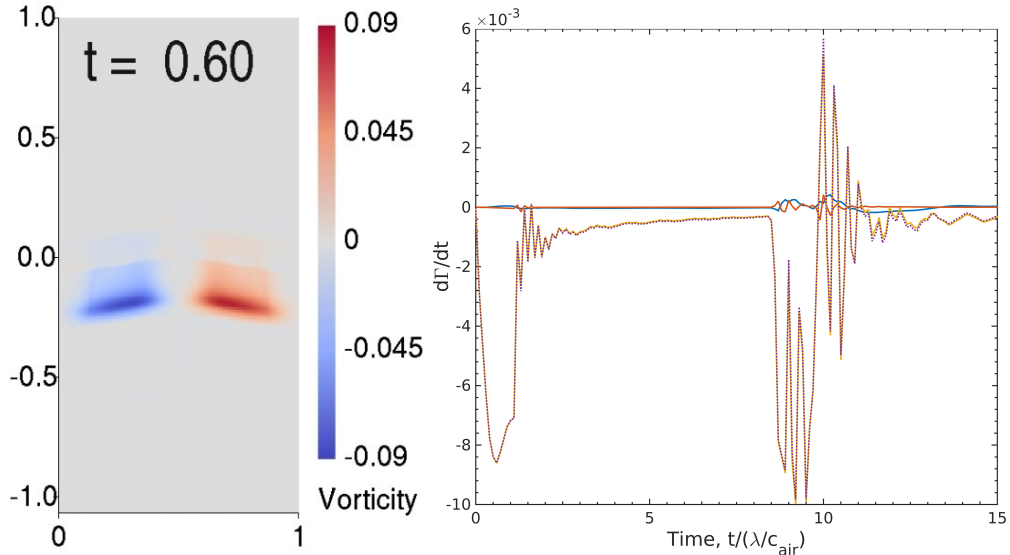


Figure 3.7: A surface plot of vorticity for the 10 MPa trapezoidal wave case, at time $t = 0.6$, during the middle of the interface-compression wave interaction (Left). Each term of the circulation generation equation (3.11) is plotted as a function of time: $(d\Gamma/dt)_{\text{advection}}$ (blue), $(d\Gamma/dt)_{\text{compressible}}$ (orange), $(d\Gamma/dt)_{\text{baroclinic}}$ (yellow), $(d\Gamma/dt)_{\text{total}}$ (purple, dotted) is plotted as a function of time (Right).

prohibitive.

3.4.4 Further discussion of the results

For both the trapezoidal and DUS pulse-like acoustic waves, the pressure, velocity, and density return to initial, ambient conditions after the passing of the wave. As these waveforms are continuous, this implies that the integral of the pressure gradient ∇p at each point along the interface, over all time must be zero. Hence we surmise that if the interface remained  unchanged during the interaction with the wave, implying constant $\nabla \rho$, the net baroclinic circulation deposited must be zero. Thus for any finite duration acoustic wave such as ours to deposit net baroclinic circulation upon an interface, the interface itself must deform during interaction with the wave. This deformation alters the misalignment of the pressure and density gradients at the interface causing positive and negative circulation deposited to not cancel out entirely. Note that this is unique to waves that begin and end at the same pressure. This is not the case for the traditional RMI problem, for which conditions do not return to their original state after the passage of the shock.

For the cases varying the length of the static elevated pressure in the trapezoidal wave we previously noted that whether the expansion increased or decreased the total half-domain cir-

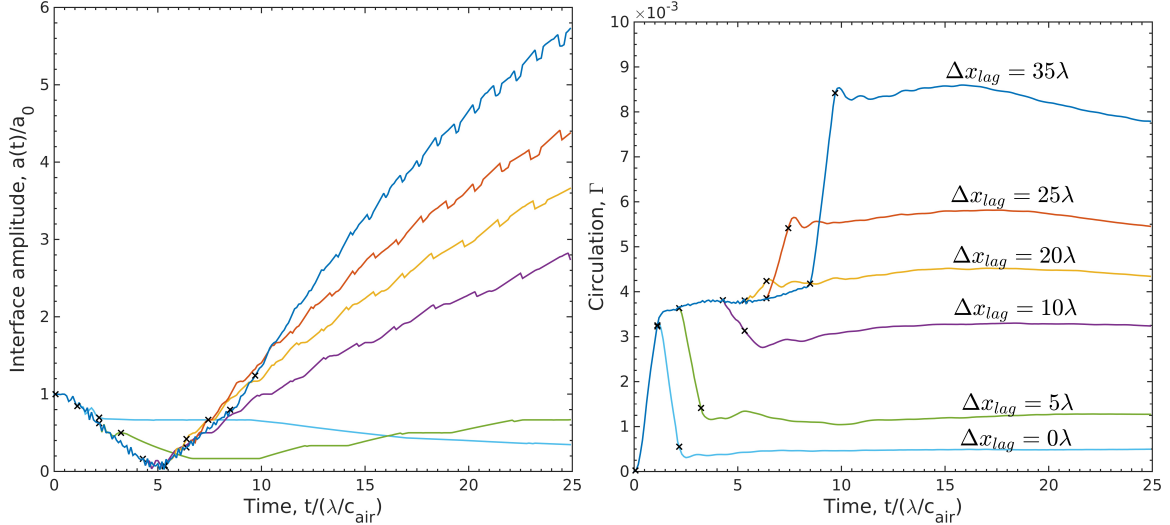


Figure 3.8: The interface amplitude (left) and circulation (right) histories for varying elevated static pressure durations or lag time Δx_{lag} between the expansion and compression waves. Here we show results for $\Delta x_{\text{lag}} = 35\lambda$ (blue), $\Delta x_{\text{lag}} = 25\lambda$ (orange), $\Delta x_{\text{lag}} = 20\lambda$ (yellow), $\Delta x_{\text{lag}} = 10\lambda$ (purple), $\Delta x_{\text{lag}} = 5\lambda$ (green), $\Delta x_{\text{lag}} = 0\lambda$ (light blue)

culation depended on whether it encountered the interface before or after the phase change. If indeed circulation is driving the deformation of the interface, then changes in the waveform that appear to have very little effect on the interface dynamics during the wave-interface interaction period, may have far more significant impacts on the long term dynamics of the interface. To put this in the context of DUS, which uses repeated pulses, if ultrasonically-deposited circulation is causing deformation within the lungs, longer Pulse Durations (PDs) may allow for greater deformation and increased circulation deposition as a result of any individual pulse. If the system acts as we have modeled it, the Pulse Repetition Frequency (PRF) would determine the degree of interface deformation experienced by pulses subsequent to the first and may influence deformation and hemorrhage. Finally, in recognition of the limitations of this study, we note that the true physical nature of lung tissue is viscoelastic ([Bayliss & Robertson, 1939](#)), and neither viscosity nor elasticity is included in our model problems. While preliminary results with a Navier-Stokes code showed similar early time results, we expect that viscosity would dissipate circulation over a long enough period of time. Furthermore, elasticity may provide a mechanism by which the alveolar walls could resist deformation or retard to their original shape between pressure perturbations.

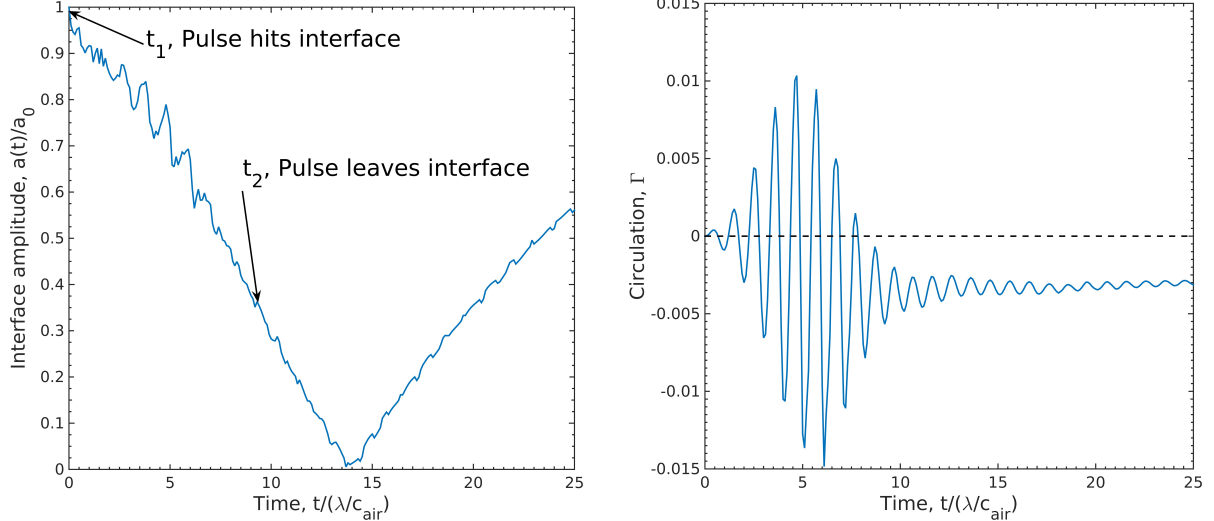


Figure 3.9: The dimensionless interface amplitude (left) and dimensionless circulation (right) histories corresponding to the a water-air interface disturbed by the US-like pulse shown in Figure 3.2.

3.5 Conclusions

This work is unique in that we propose a previously unconsidered potential damage mechanism for DUS-induced LH. We hypothesize that baroclinic torque occurs at fragile air-tissue interfaces of the lung due to misalignment between the US pressure gradient and material interface density gradient, causing stress, deformation, and ultimately rupture at the interface. This mechanism arises as a result of nonlinear, compressible fluid mechanics, and cannot be predicted through traditional linear acoustics. We suggest that nonlinear effects such as baroclinic vorticity are important to this problem because of the sharp density discontinuities between air and tissue within the lungs. To investigate our hypothesis we develop a numerical model of DUS wave-alveolus interaction and simulate the physics underlying acoustically driven, perturbed liquid-gas interfaces.

We aim to investigate three specific questions presented in Section 3.3. To address these questions, we enumerate three conclusions of this work based on our results. First, acoustic waves can generate vorticity at perturbed liquid-gas interfaces as a result of baroclinic torque. Second, this vorticity is capable of appreciably deforming the interface in the inviscid, inelastic case. We note that at this preliminary stage, additional simulations, run for longer time, will be useful in solidifying this conclusion. Third, acoustic properties relevant to DUS including acoustic amplitude, wave duration, and repetition frequency, are important to circulation deposition and subsequently any circulated-driven deformation or hemorrhage. For the case of

a simple trapezoidal pressure wave, we demonstrate that the amount of circulation deposited along the interface scales linearly with the acoustic pressure amplitude. More subtly, because the interface is deforming throughout its interaction with the wave, affecting the alignment of pressure and density gradients, the acoustic wave duration can play an important role in determining how much circulation is ultimately deposited. Because the deformation can continue long after the wave has gone, similar arguments can be made for timing between subsequent waves. With regard to ultrasound, this could play an important role in choosing optimal PD and PRF.

3.6 Future Work

Finally, we address some of the limitations of this study and propose future work to address some of these issues. To further evaluate the relevance of the proposed damage mechanisms and presented results to DUS-induced lung hemorrhage, viscous and elastic effects should be considered, as both of these have the potential to reduce observed deformation, and mitigate hemorrhage. Additionally, more realistic geometries that more accurately represent physical networks of alveoli within the lungs will be useful to understand the propagation of ultrasound waves and hemorrhage deeper into the lungs, beyond the first tissue, air interface. To do this accurately, it may be necessary to include a model for interface rupture. Many of these future tasks will require not only additional numerical efforts, but also experimental studies to appropriately characterize the lung tissue and validate the suggested models. Additionally, to increase our understanding of the relevant fluid dynamics, it will be important it would be useful to be able predict the circulation and interface dynamics based on the wave properties and initial conditions.

To address some of these issues and complete the proposed dissertation research we plan to perform several tasks:

- To further the relevance of this research to the problem of DUS of the lung we will:
 1. Calculate the relevant viscous stresses based on computed velocity gradients and interface strains and compare to known properties of the lung.
 2. Investigate the effects of alveolar wall structures by combine periodic boundary conditions with thin water walls at the edges of the air.
 3. Investigate the propagation of ultrasound waves and hemorrhage into the lungs by using appropriate cyclic water-air-water geometries.

- To further our understanding of fluid mechanics associated with acoustically perturbed fluid interfaces we will:
 1. Perform longer simulations to validate $a(t) \sim \sqrt{\Gamma t}$ scaling.
 2. Develop a model to predict the circulation deposited on a slightly perturbed interface by a simple compression or expansion wave.
 3. Develop a model to predict the interface phase-reversal time for a simple compression wave.
 4. Design acoustic waveforms that utilize time dependent features and interface deformation to generate minimal circulation and interface growth.
 5. Investigate the cause of late time circulation growth observed in some simulations.
 6. Investigate the dependence of circulation on the type of Riemann solver used.



Part II

**Estimating transmission loss uncertainty
in uncertain ocean environments.**

CHAPTER 4

Past work: Efficient estimation of the probability density function of transmission loss in uncertain ocean environments via area statistics

In this chapter we present the highlights of past work in which we develop and test a computationally efficient method for predicting acoustic Transmission Loss (TL) in uncertain ocean environments. This work was presented at the 169TH meeting of the Acoustical Society in Pittsburgh, PA on May 28, 2015 ([Patterson & Dowling, 2015](#)) and submitted for review to the Journal of the Acoustical Society of America on February 22, 2016. Here we present the abstract, key figures, and conclusions of the submitted work.

4.0.1 Abstract

Calculations of acoustic TL in the ocean are useful in naval and ocean monitoring applications. These TL calculations are often uncertain because they are based on uncertain environmental parameters, but standard methods for determining TL uncertainty are computationally expensive. This paper describes how TL statistics in a range-depth area surrounding the point of interest within a single TL-field calculation can be efficiently used to estimate the Probability Distribution Function (PDF) of TL that results from ocean environment uncertainty. Such area-statistics estimated PDFs of TL are compared to PDFs of TL obtained from 1000-sample Monte-Carlo calculations at source frequencies of 100, 200 and 300 Hz and source depths of 91, 137, and 183 m in four different uncertain ocean environments at test location depths from 20 m to 5 km and source-receiver ranges from a few km to more than 60 km. These comparisons show that the estimated PDFs of TL are engineering-level accurate in 93% of tests in ocean environments with consistent bottom reflection, and can be produced with $O(10^{-6})$ the

computational effort required for the Monte-Carlo calculations. In deep refracting environments, area statistics was engineering-level in 78% of test cases after algorithm adjustments.

4.1 Key figures

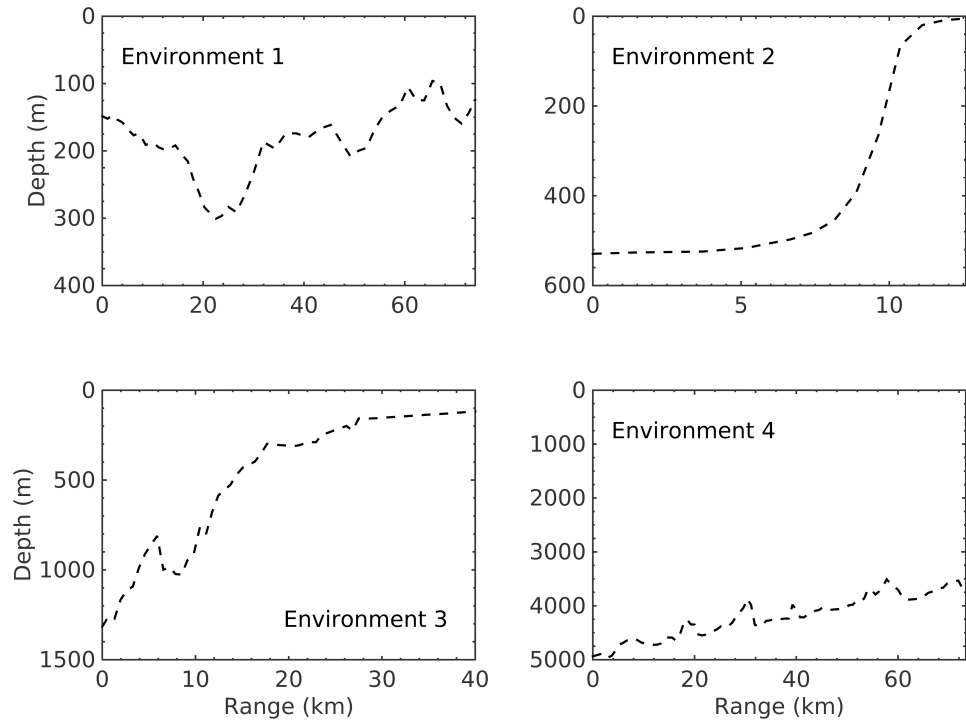


Figure 4.1: Nominal bathymetry of the four uncertain ocean environments used in this study. The ordering goes from shallowest (1) to deepest (4).

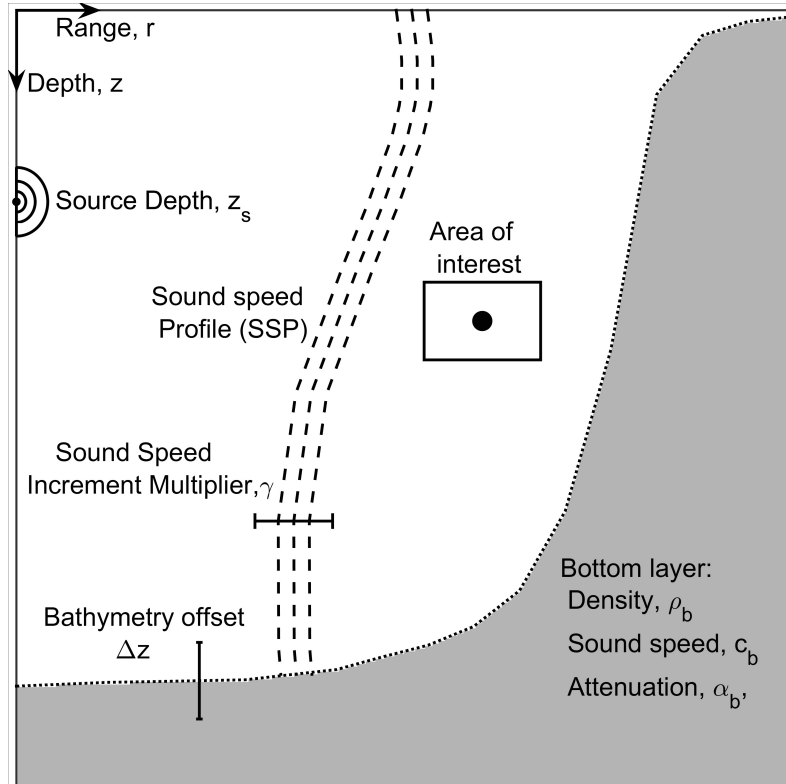


Figure 4.2: Generic range-dependent ocean environment with five uncertain parameters: bathymetry offset Δz ; sound speed increment multiplier γ ; and seabed properties (density ρ_b , sound speed c_b , attenuation coefficient α_b). Here, all five are assumed to be range independent. The source depth is a constant $z_s = 137$ m. The point of interest for recovering the PDF of TL is indicated by a black dot. The rectangle surrounding this dot nominally indicates the range-depth area utilized by the area statistics technique.

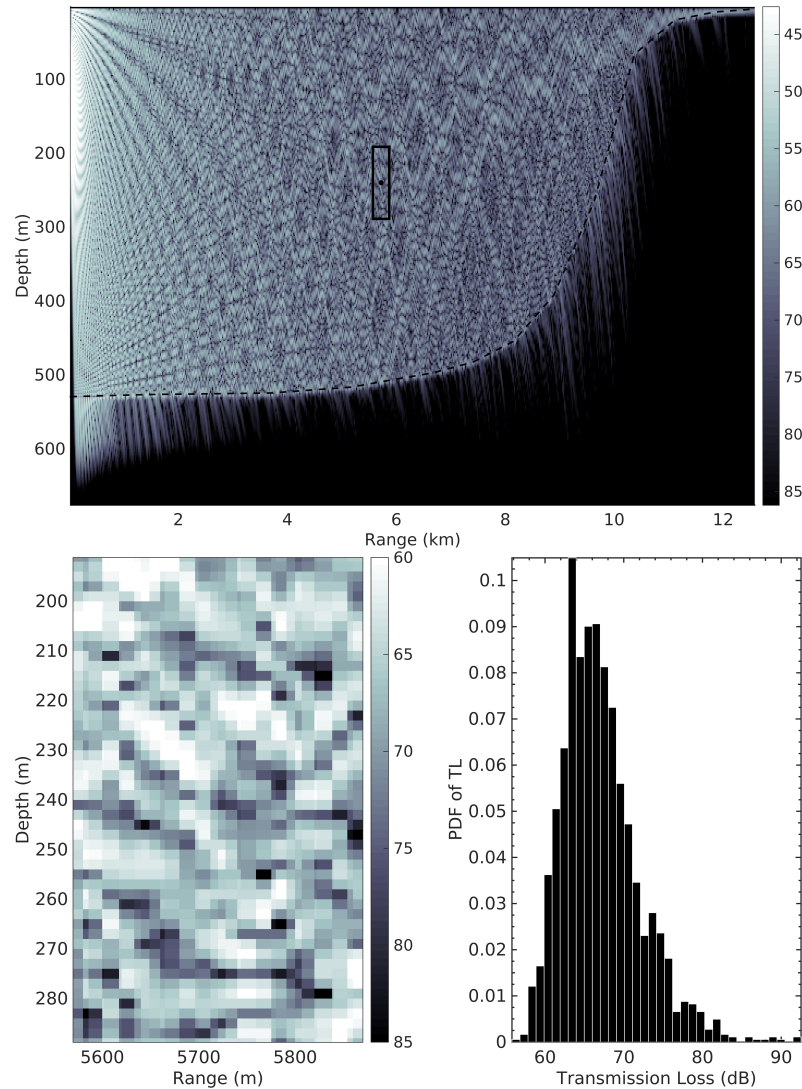


Figure 4.3: (Top) Example TL field for a $f_s = 200$ Hz source in environment 2 with a $40\lambda_s \times 10\lambda_s$ (*rangexdepth*) area statistics sample area centered at range-depth location $r = 5720$ m, $z = 240$ m. (Bottom-left) Expanded area statistics TL sample rectangle from the TL field shown above. (Bottom-right) PDF of TL generated from the TL values collected in the sample area.

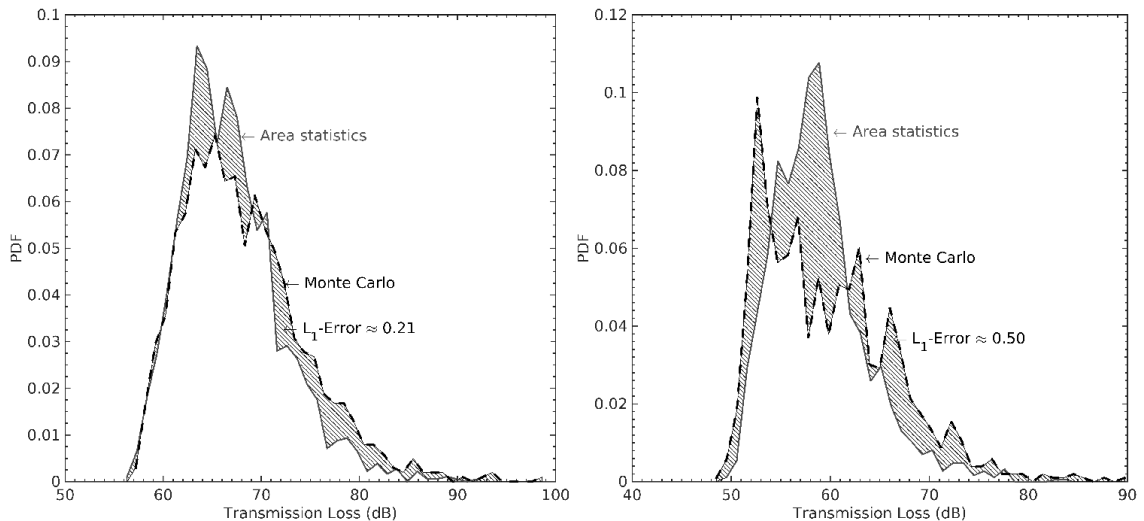


Figure 4.4: Comparison of area-statistics (solid curve) and MC (dashed curve) generated PDFs of TL in environment 2 at $r = 5720$ m and $z = 288$ m (a), and $r = 1140$ m and $z = 384$ m. In both panels, the L_1 -error is the jagged marked area. (Left) $L_1 = 0.21$. With the MC PDF assumed to be correct, the mean and standard deviation errors of the area statistics PDF is 1.23 dB and 1.02 dB, respectively. (Right) $L_1 = 0.503$. The mean and standard deviation errors are 0.86 dB and 1.92 dB, respectively. The area- statistics-estimated PDF of TL on the left is considered engineering-level accurate while that on the right is not.

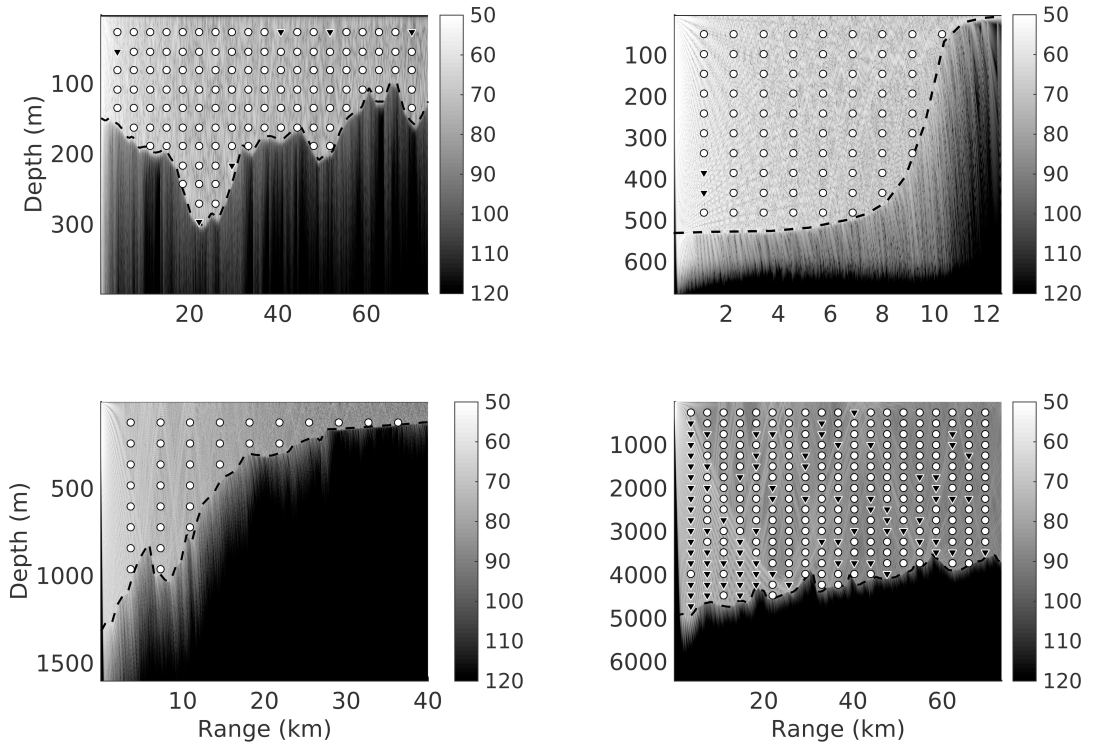


Figure 4.5: TL fields for the four environments shown in Figure 4.1 with a $f_s = 200$ Hz source and markers indicating locations where area statistics and MC generated PDFs of TL were compared. White circles indicate locations where area-statistics results compare favorably with those from MC calculations ($L_1 \leq 0.50$). Black triangles indicate locations where such comparisons are unfavorable ($L_1 \geq 0.50$).

4.2 Conclusions

This paper describes the area statistics technique for efficiently estimating TL uncertainty in underwater acoustics. The technique is based on the idea that the TL variation found near the point interest in real space is similar to that found at the location of interest when environmental parameters are varied. The technique is simple and can be used to produce approximate PDFs of TL in uncertain ocean sound channels from a single (baseline) TL field calculation completed using the most probable value for each uncertain parameter. To implement the technique, TL values near a location of interest in the baseline TL field are collected and sorted into a histogram that is normalized to obtain an approximate PDF of TL at the location of interest. To determine the technique's accuracy, PDFs of TL created using area statistics were compared to PDFs generated using 1000-sample MC calculations in four different ocean environments at three acoustic frequencies ($f_s = 100, 200, \text{ and } 300 \text{ Hz}$) for three different source depths ($z_s = 91, 137, \text{ and } 183 \text{ m}$). The area-statistics PDFs of TL achieved engineering-level accuracy ($L_1 \leq 0.5$) in 93% of test cases in the three shallower environments with consistent bottom reflection. In the environments where refraction was more important, area statistics was less successful; engineering level accuracy was only achieved in 56% of test cases, initially. However, this success percentage was improved to 65% by gently modifying the area statistics algorithm, and this modification did not affect the results in the shallower ocean environments.

The effort reported here supports the following four conclusions. (1) The area statistics technique is a viable alternative, or worthy complement, to MC calculations or other more computationally intensive techniques for estimating the uncertainty of TL field calculations in uncertain ocean environments with consistent downward-refraction and bottom reflection. In each of the three environments of this investigation meeting this bottom reflection criterion, the technique produced engineering-level accuracy at 85% or more of the test locations. (2) The area statistics algorithm is simple enough that it can be modified to improve the technique's overall performance. One simple algorithm adjustment improved the engineering accuracy success rate of area statistics in the deepest environment considered in this study by approximately 10% at all three frequencies. (3) The area statistics technique is so inexpensive computationally that it should be implemented even when a more reliable but more computationally demanding approach is the primary means for TL uncertainty estimation. As part of this investigation, the area statistics approach was found to be millions of times faster than MC calculations. Thus, the computational penalty for implementing both, if the latter is preferred, is vanishingly small. Moreover, the technique is computationally inexpensive enough

for use in real time applications. (4) The sample rectangle size, TL sample weighting, and other implementation details of the area statistics algorithm described here are likely to need adjustment if the ocean sound channel uncertainties of interest differ from those considered. The area statistics technique is ad-hoc and the implementation parameters in its current formulation were tuned to achieve a high percentage of engineering-accurate predictions for ocean sound channels with the uncertainties considered. However, the uncertainties considered are generic and may serve as a useful starting point for many uncertain ocean sound channels. Thus, the area statistics formulation provided here may be broadly applicable.

BIBLIOGRAPHY

- Apfel, R E, & Holland, C K. 1991. Gauging the likelihood of cavitation from short-pulse, low-duty cycle diagnostic ultrasound. *Ultrasound in medicine & biology*, **17**(2), 179–185.
- Baggs, R., Penney, D.P., Cox, C., Child, S.Z., Raeman, C.H., Dalecki, D., & Carstensen, E.L. 1996. Thresholds for ultrasonically induced lung hemorrhage in neonatal swine. *Ultrasound in Medicine & Biology*, **22**(1), 119–128.
- Bayliss, L. E., & Robertson, G. W. 1939. THE VISCO-ELASTIC PROPERTIES OF THE LUNGS. *Quarterly Journal of Experimental Physiology and Cognate Medical Sciences*, **29**(1), 27–47.
- Brouillette, Martin. 2002. The Richtmyer-Meshkov Instability. *Annual Review of Fluid Mechanics*, **34**(1), 445–468.
- Child, S.Z., Hartman, C.L., Schery, L.A., & Carstensen, E.L. 1990. Lung damage from exposure to pulsed ultrasound. *Ultrasound in Medicine & Biology*, **16**(8), 817–825.
- Dalecki, Diane, Child, Sally Z., Raeman, Carol H., Cox, Christopher, & Carstensen, Edwin L. 1997. Ultrasonically induced lung hemorrhage in young swine. *Ultrasound in Medicine and Biology*, **23**(5), 777–781.
- Drake, Paul. 2006. *High-Energy-Density Physics*. Shock Wave and High Pressure Phenomena. Springer Berlin Heidelberg.
- Edelman, Sidney. 2005. *Understanding ultrasound physics*. Woodlands, Texas: ESP.
- Frizzell, Leon a., Chen, Ellen, & Lee, Chong. 1994. Effects of pulsed ultrasound on the mouse neonate: Hind limb paralysis and lung hemorrhage. *Ultrasound in Medicine and Biology*, **20**(1), 53–63.
- Frizzell, Leon A., Zachary, James F., O'Brien, William D., & O'Brien, William D. 2003. Effect of pulse polarity and energy on ultrasound-induced lung hemorrhage in adult rats. *The Journal of the Acoustical Society of America*, **113**(5), 2912.
- Harrison, G.H. H, Eddy, H.A. A, Wang, J.-P. P, & Liberman, F.Z. Z. 1995. Microscopic lung alterations and reduction of respiration rate in insonated anesthetized swine. *Ultrasound in medicine & biology*, **21**(7), 981–983.

- Henry de Frahan, Marc T., Varadan, Sreenivas, & Johnsen, Eric. 2015. A new limiting procedure for discontinuous Galerkin methods applied to compressible multiphase flows with shocks and interfaces. *Journal of Computational Physics*, **280**(jan), 489–509.
- Holland, Christy K., Deng, Cheri X., Apfel, Robert E., Alderman, Jonathan L., Fernandez, Leonardo A., & Taylor, Kenneth J.W. 1996. Direct evidence of cavitation in vivo from diagnostic ultrasound. *Ultrasound in Medicine & Biology*, **22**(7), 917–925.
- Kinsler, Lawrence E., Frey, Austin R., Coppens, Alan B., & Sanders, James V. 1982. Fundamentals of Acoustics by Lawrence. *The Journal of the Acoustical Society of America*, **72**(3), 1090.
- Kramer, J. M., Waldrop, T. G., Frizzell, L. A., Zachary, J. F., & O'Brien, W D. 2001. Car-diopulmonary function in rats with lung hemorrhage induced by pulsed ultrasound exposure. *Journal of ultrasound in medicine : official journal of the American Institute of Ultrasound in Medicine*, **20**(11), 1197–1206.
- Lichtenstein, Daniel A. 2009. Ultrasound examination of the lungs in the intensive care unit. *Pediatric critical care medicine : a journal of the Society of Critical Care Medicine and the World Federation of Pediatric Intensive and Critical Care Societies*, **10**(6), 693–698.
- Meltzer, Richard S., Adsumelli, Rishi, Risher, William H., Hicks, George L., Stern, David H., Shah, Pratima M., Wojtczak, Jacek A., Lustik, Stewart J., Gayeski, Thomas E., Shapiro, Janine R., & Carstensen, Edwin L. 1998. Lack of Lung Hemorrhage in Humans After Intraoperative Transesophageal Echocardiography with Ultrasound Exposure Conditions Similar to Those Causing Lung Hemorrhage in Laboratory Animals. *Journal of the American Society of Echocardiography*, **11**(1), 57–60.
- Miller, Douglas L, Dou, Chunyan, & Wiggins, Roger C. 2008. Frequency Dependence of Kidney Injury Induced by Contrast-Aided Diagnostic Ultrasound in Rats. *Ultrasound in Medicine & Biology*, **34**(10), 1678–1687.
- O'Brien, W.D., Jr., Simpson, D.G., Frizzell, L.a., & Zachary, J.F. 2001a. Age-dependent threshold and superthreshold behavior of ultrasound-induced lung hemorrhage in pigs. *2001 IEEE Ultrasonics Symposium. Proceedings. An International Symposium (Cat. No.01CH37263)*, **2**(6).
- O'Brien, W D, Frizzell, Leon A., Weigel, Ronald M., Zachary, James F., O'Brien, William D., Frizzell, Leon A., Weigel, Ronald M., & Zachary, James F. 2000. Ultrasound-induced lung hemorrhage is not caused by inertial cavitation. *The Journal of the Acoustical Society of America*, **108**(3), 1290–1297.
- O'Brien, W.D., Simpson, D.G., Frizzell, L.A., & Zachary, J.F. 2001b. Superthreshold behavior and threshold estimates of ultrasound-induced lung hemorrhage in adult rats: role of beamwidth. *IEEE Transactions on Ultrasonics, Ferroelectrics and Frequency Control*, **48**(6), 1695–1705.

- O'Brien, W.D., Simpson, D.G. Douglas G, Moon-Ho Ho, Miller, R.J. Rita J, Frizzell, Leon A L.A., Zachary, James F J.F., Brien, William D O, Simpson, D.G. Douglas G, Ho, Moon-ho, Miller, R.J. Rita J, Frizzell, Leon A L.A., Member, Senior, & Zachary, James F J.F. 2003a. Superthreshold behavior and threshold estimation of ultrasound-induced lung hemorrhage in pigs: Role of age dependency. *IEEE Transactions on Ultrasonics, Ferroelectrics and Frequency Control*, **50**(2), 153–169.
- O'Brien, William D, Frizzell, Leon A, Schaeffer, David J, & Zachary, James F. 2001c. Superthreshold behavior of ultrasound-induced lung hemorrhage in adult mice and rats: role of pulse repetition frequency and exposure duration. *Ultrasound in Medicine & Biology*, **27**(2), 267–277.
- O'Brien, William D., Kramer, Jeffrey M., Waldrop, Tony G., Frizzell, Leon A., Miller, Rita J., Blue, James P., & Zachary, James F. 2002. Ultrasound-induced lung hemorrhage: Role of acoustic boundary conditions at the pleural surface. *The Journal of the Acoustical Society of America*, **111**(2), 1102.
- O'Brien, William D., Simpson, Douglas G., Frizzell, Leon a., & Zachary, James F. 2003b. Threshold estimates and superthreshold behavior of ultrasound-induced lung hemorrhage in adult rats: Role of pulse duration. *Ultrasound in Medicine and Biology*, **29**(11), 1625–1634.
- O'Brien, William D., Simpson, Douglas G., Frizzell, Leon A., & Zachary, James F. 2005. Superthreshold behavior of ultrasound-induced lung hemorrhage in adult rats: Role of pulse repetition frequency and exposure duration revisited. *Journal of Ultrasound in Medicine*, **24**(3), 339–348.
- O'Brien, William D. W.D., & Zachary, J.F. 1997. Lung damage assessment from exposure to pulsed-wave ultrasound in the rabbit, mouse, and pig. *IEEE Transactions on Ultrasonics, Ferroelectrics and Frequency Control*, **44**(2), 473–485.
- O'Brien, William D., Jr, Simpson, Douglas G., Frizzell, Leon A., & Zachary, James F. 2006. Superthreshold Behavior of Ultrasound-Induced Lung Hemorrhage in Adult Rats: Role of Pulse Repetition Frequency and Pulse Duration. *J. Ultrasound Med.*, **25**(7), 873–882.
- Patterson, Brandon, & Dowling, David R. 2015. Efficient estimation of the probability density function of transmission loss in uncertain ocean environments. *Journal of the Acoustical Society of America*, **137**(4), 2439–2439.
- Patterson, Brandon, Miller, Douglas, & Johnsen, Eric. 2012. Theoretical microbubble dynamics in a homogeneous viscoelastic medium at capillary breaching thresholds. *The Journal of the Acoustical Society of America*, **131**(4), 3385–3385.
- Penney, D.P., Schenk, E.A., Maltby, K., Hartman-Raeman, C., Child, S.Z., & Carstensen, E.L. 1993. Morphological effects of pulsed ultrasound in the lung. *Ultrasound in Medicine & Biology*, **19**(2), 127–135.

- Raeman, Carol H., Child, Sally Z., & Carstensen, Edwin L. 1993. Timing of exposures in ultrasonic hemorrhage of murine lung. *Ultrasound in Medicine & Biology*, **19**(6), 507–512.
- Raeman, C.H., Child, S.Z., Dalecki, D., Cox, C., & Carstensen, E.L. 1996. Exposure-time dependence of the threshold for ultrasonically induced murine lung hemorrhage. *Ultrasound in Medicine & Biology*, **22**(1), 139–141.
- Tarantal, Alice F., & Canfield, Don R. 1994. Ultrasound-induced lung hemorrhage in the monkey. *Ultrasound in medicine & biology*, **20**(1), 65–72.
- Tjan, K. K., & Phillips, W. R. C. 2007 (mar). *On impulsively generated inviscid axisymmetric surface jets, waves and drops*.
- Tjan, K.K., & Phillips, W.R.C. 2008. On the impulsive generation of drops at the interface of two inviscid fluids. *Proceedings of the Royal Society A: Mathematical, Physical and Engineering Sciences*, **464**(2093), 1125–1140.
- Yang, Xinmai, & Church, Charles C. 2005. A model for the dynamics of gas bubbles in soft tissue. *The Journal of the Acoustical Society of America*, **118**(6), 3595–3606.
- Zachary, J. F., & O'Brien, W. D. 1995. Lung Lesions Induced by Continuous- and Pulsed-Wave (Diagnostic) Ultrasound in Mice, Rabbits, and Pigs. *Veterinary Pathology*, **32**(1), 43–54.
- Zachary, James F., Frizzell, Leon a., Norrell, Kandice S., Blue, James P., Miller, Rita J., O'Brien, William D., & O'Brien, William D. 2001a. Temporal and spatial evaluation of lesion reparative responses following superthreshold exposure of rat lung to pulsed ultrasound. *Ultrasound in Medicine and Biology*, **27**(6), 829–839.
- Zachary, James F., Blue, James P., Miller, Rita J., Ricconi, Brian J., Eden, J. Gary, & O'Brien, William D. 2006. Lesions of ultrasound-induced lung hemorrhage are not consistent with thermal injury. *Ultrasound in Medicine and Biology*, **32**(11), 1763–1770.
- Zachary, J.F., Sempsrott, J.M., Frizzell, L.A., Simpson, D.G., & O'Brien, W.D. 2001b. Superthreshold behavior and threshold estimation of ultrasound-induced lung hemorrhage in adult mice and rats. *IEEE Transactions on Ultrasonics, Ferroelectrics and Frequency Control*, **48**(2), 581–592.